INL/EXT-15-36735

Light Water Reactor Sustainability Program

Advanced Seismic Fragility Modeling using Nonlinear Soil-Structure Interaction Analysis

Chandu Bolisetti
Justin Coleman
Mohamed Talaat
Philip Hashimoto

September 2015

U.S. Department of Energy
Office of Nuclear Energy

INL/EXT-15-36735

Advanced Seismic Fragility Modeling using Nonlinear Soil-Structure Interaction Analysis

Chandu Bolisetti and Justin Coleman, Idaho National Laboratory
Mohamed Talaat and Philip Hashimoto, Simpson-Gumpertz & Heger

September 2015

Idaho National Laboratory
Nuclear Science & Technology
Idaho Falls, Idaho 83415

http://www.inl.gov

Prepared for the
U.S. Department of Energy
Office of Nuclear Energy
Under DOE Idaho Operations Office
Contract DE-AC07-05ID14517

EXECUTIVE SUMMARY

The goal of this effort is to compare the seismic fragilities of a nuclear power plant system obtained by a traditional seismic probabilistic risk assessment (SPRA) and an advanced SPRA that utilizes Nonlinear Soil-Structure Interaction (NLSSI) analysis. Soil-structure interaction (SSI) response analysis for a traditional SPRA involves the linear analysis, which ignores geometric nonlinearities (i.e., soil and structure are glued together and the soil material undergoes tension when the structure uplifts). The NLSSI analysis will consider geometric nonlinearities.

Risk calculations should focus on providing best estimate results, and associated insights, for evaluation and decision-making. Specifically, seismic probabilistic risk assessments (SPRAs) are intended to provide best estimates of the various combinations of structure and equipment failures that can lead to a seismic-induced core damage event. However, in some instances, the current SPRA approach has large uncertainties, and potentially masks other important events.

SPRA's are performed by convolving the seismic hazard (this is the estimate of all likely damaging earthquakes at the site of interest) with the seismic fragility (the conditional probability of failure of a structure, system, or component given the occurrence of earthquake ground motion). In this calculation, there are three main pieces to seismic risk quantification, 1) seismic hazard and nuclear power plants (NPPs) response to the hazard, fragility or capacity of structures, systems and components (SSC), and systems analysis.

Two areas where nonlinear effects may be important in SPRA calculations are, 1) calculation of in-structure response at the area of interest, and 2) calculation of seismic fragilities (current fragility calculations assume a lognormal distribution for the conditional probability of failure of components).

The focus of the research task presented herein is on implementation of NLSSI into the SPRA calculation process when calculating in-structure response at the area of interest. The specific nonlinear soil behavior included in the NLSSI calculation presented in this report is gapping and sliding. Other NLSSI effects are not included in the calculation. The results presented in this report provide preliminary and approximate comparisons of fragilities calculated using a traditional SPRA assumption that in-structure response scales linearly with increasing ground motion with fragilities calculated by removing this assumption and by considering gapping and sliding.

A comparison of the response distributions showed that the median demands calculated considering the nonlinear effects do not scale linearly unlike in traditional SPRA. A comparison between the component fragilities showed that the conditional probabilities of failure for given PGA values estimated using advanced SPRA are generally smaller than those calculated using the traditional approach.

CONTENTS

ACRONYMS

DBE	Design Basis Earthquake
DOE	Department of Energy
INL	Idaho National Laboratory
NLSSI	Nonlinear Soil Structure Interaction
NNSA	National Nuclear Security Administration
NRC	Nuclear Regulatory Commission
SASSI	System for Analysis of Soil Structure Interaction
SCDF	Seismic Core Damage Frequency
SSI	Soil-Structure Interaction

1. Introduction

1.1 Overview

The estimate of the seismic hazard at nuclear facilities continues to evolve and generally leads to an increase in the hazard. The change in understanding of the site-specific seismic hazard curve occurs as more information is gathered on seismic sources and events, and additional research is performed to update attenuation relationships and characterize local site effects. As the seismic hazard increases, more intense input ground motions are used to numerically evaluate nuclear facility response. This results in higher soil strains, increased potential for gapping and sliding and larger in-structure responses. Therefore, as the intensity of ground motions increases, the importance of capturing nonlinear effects in numerical SSI models increases.

The goal of this effort is to compare the seismic fragilities obtained by a traditional nuclear power plant seismic probabilistic risk assessment (SPRA) and an advanced SPRA that utilizes Nonlinear Soil-Structure Interaction (NLSSI) analysis. Soil-structure interaction (SSI) analysis in traditional SPRA involves ignoring the geometric properties (soil and structure are glued together, namely, the soil undergoes tension when structure uplifts), and using linear soil properties and linear structure properties. The NLSSI analysis of this study will consider geometric nonlinearities, namely, gapping and sliding of the foundation.

The focus of the research task presented herein is on the implementation of NLSSI into the SPRA calculation process when calculating in-structure response at the area of interest. The specific nonlinear soil behavior included in the NLSSI calculation presented in this report is gapping and sliding. Other NLSSI effects are not included in the calculation. The commercial software program, LS-DYNA, is used for the NLSSI analyses.

The results presented in this report are used to approximate trends in seismic fragility behavior when using NLSSI. Only a limited number of NLSSI analyses were performed. The resulting seismic fragilities are considered to be approximate and are intended only to provide an initial comparison to seismic fragilities obtained from linear analysis. A larger sample of NLSSI analyses is currently being performed to permit a more rigorous quantification of seismic fragilities. These analyses and the resulting fragilities will be documented in a future report.

1.2 External hazard analysis

This report documents an approach or methodology for incorporating advanced seismic NLSSI tools in a risk-informed framework. This fits within the vision to advance external hazards analysis. The vision of performing advanced external hazard (in this report seismic is presented, future efforts will couple seismic and flooding) risk-informed margins management is using verified and validated tools and methods that provide best estimate nuclear facility response, with quantified uncertainties, and ensures plant safety during and after beyond design basis events.

The vision will be completed in the short, medium, and long term by accomplishing to following goals:

Short Term Goal

Provide DOE and Industry with verified and validated analytical methods and to evaluate larger seismic ground motions at critical infrastructure and nuclear facilities and implement protective measures such as seismic isolation (SI). The goal is to minimize seismic risk at nuclear facilities through cost-effective analytical approaches and technologies.

Long Term Goal

Development of advanced methods and tools to evaluate the performance of virtual nuclear power plants and nuclear facilities to a wide range of external hazards including multiple event scenarios allowing nuclear facility owners to virtually test external hazards before the actual facilities are tested with actual hazards, and to anticipate potential issues and resolve them.

The long-term goal will be accomplished by incorporating structural dynamics capabilities in the MOOSE framework (since this framework has access to numerical tools that can quantify reactor core behavior). Structural dynamic numerical development is documented in Appendix A.

2. Problem Description

2.1 Representative soil site and nuclear power plant structure

This study uses a soil profile representing the basalt under the Advanced Test Reactor (ATR) located at INL. The soil properties listed in Table 3-1 is considered to be uniform with depth. Excluding soil damping, these values were used in the TRA-670 SPRA.

Table 2-1: Soil properties

Property	**Median**	**Lognormal Std. Deviation**
Unit weight	159 lb/ft^3	-
Poisson's ratio	0.35	-
Shear-wave velocity	3720ft/sec	0.27
Shear modulus	68,320 kip/ft^2	0.55
Damping	2%	0.4

The selected representative NPP structure is a pressurized water reactor building. The numerical model of this structure is obtained from the SASSI2000 user manual. It consists of a pre-stressed concrete containment structure and a reinforced concrete internal structure. The numerical models of both the containment and internal structures are idealized stick models illustrated in the left panel of Figure 2-1. Median values of lumped masses and section properties of the stick models are presented in the right panel of this figure. These lumped masses include the masses of the stick elements apart from the masses of the non-structural components at each level. Therefore a zero mass density is assigned for the concrete material in the internal and containment structures. A median elastic modulus of 6.9×10^5 ksf and a median shear modulus of 2.7×10^5 ksf are assumed for the concrete material. However the concrete modulus of the internal structure is reduced by a factor of 0.5 to obtain a fundamental frequency near the peak of the UHS and therefore amplify the structural response. The CLASSI model of the representative NPP structure is identical to this SASSI2000 model.

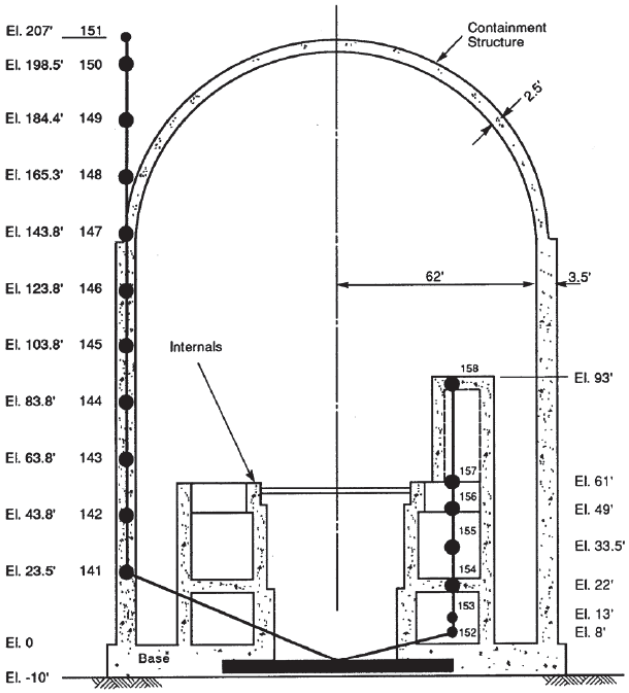

Joint Properties			Member Properties			
Mass No.	Mg (kips)		Location between Joint No.	Area (ft^2)	Shear Area (ft^2)	Moment of Inertia x 10^{-6} (ft^4)
base	20000	C				
1	46000	O	base to 1	1400	700	2.8
3	4200	N	1 to 2	1400	700	2.8
4	4200	T	3 to 4	1400	700	2.8
5	4200	A	4 to 5	1400	700	2.8
6	4200	I	5 to 6	1400	700	2.8
7	4610	N	6 to 7	1400	700	2.8
8	3020	M	7 to 8	990	500	1.9
9	2470	E	8 to 9	990	500	1.5
10	2120	N	9 to 10	990	500	0.8
11	190	T	10 to 11	990	500	0.2
12	2800	I	base to 12	2000	1320	1.1
13	2510	N	12 to 13	2560	1560	1.2
14	6290	T	13 to 14	2210	1460	1.2
15	3760	E	14 to 15	1960	730	1.3
16	8540	R	15 to 16	1740	600	0.9
17	1220	N	16 to 17	780	360	0.2
18	820	A	17 to 18	190	70	0.004

Figure 2-1: Illustration of the representative NPP structures and the corresponding stick models (left) and section properties and lumped masses of the stick model (right)[a] (Ostadan, 2006)

Table 2-2: Frequencies and percentages of total mass participation of significant modes

Mode	Frequency (Cyc/sec)	Mass participation (% of total)			Description
		UX	UY	UZ	
1, 2	5.27	45.6%	45.6%		1st horizontal mode for containment
3, 4	8.46	9.2%	9.2%		1st horizontal mode for internals
5, 6	12.37	20.4%	20.4%		2nd horizontal mode for internals
7	15.64			50.7%	1st vertical mode for containment
8, 9	16.24	9.4%	9.4%		2nd horizontal mode for containment
10	27.83			32.4%	1st vertical mode for internals
13, 14	32.89	7.9%	7.9%		3rd horizontal mode for internals

[a] The lumped mass value of mass no. 3 is 4600 kips and not 46000, and mass no. 2, which is omitted in the table is equal to 4200 kips.

2.2 Seismic hazard and input ground motions

The earthquake ground motion is based on the seismic hazard for an existing NPP. Figure 3-1 shows the seismic hazard curve expressed in terms of the horizontal peak ground acceleration (PGA) and associated mean annual frequency of exceedance (MAFE). The Reference Earthquake for the traditional SPRA seismic fragility evaluation is nominally defined as the uniform hazard spectra (UHS) at a horizontal PGA of 0.4g. This PGA corresponds to a MAFE of 1.0E-04. Figure 3-2 shows these 5% damped horizontal and vertical Reference Earthquake UHS. As a simplification for this study, the shape of the UHS is considered to be invariant with MAFE. This study uses a suite of thirty sets of earthquake ground motion time histories compatible with the Reference Earthquake UHS. The horizontal time histories account for variability of the spectral acceleration in any arbitrary direction about the geomean of the two horizontal components. Figures 3-3 to 3-5 show the 5% damped response spectra for the horizontal and vertical time histories and the target mean 1.0E-04 UHS.

INL is performing a number of NLSSI analyses at multiple ground motion levels, expected to range from 3 to 5. Each ground motion intensity level is defined by a PGA, since the UHS shapes are assumed to be constant. The reference ground motion sets are scaled to generate multiple suites using the ratios of the ground motion level PGAs to the Reference Earthquake PGA.

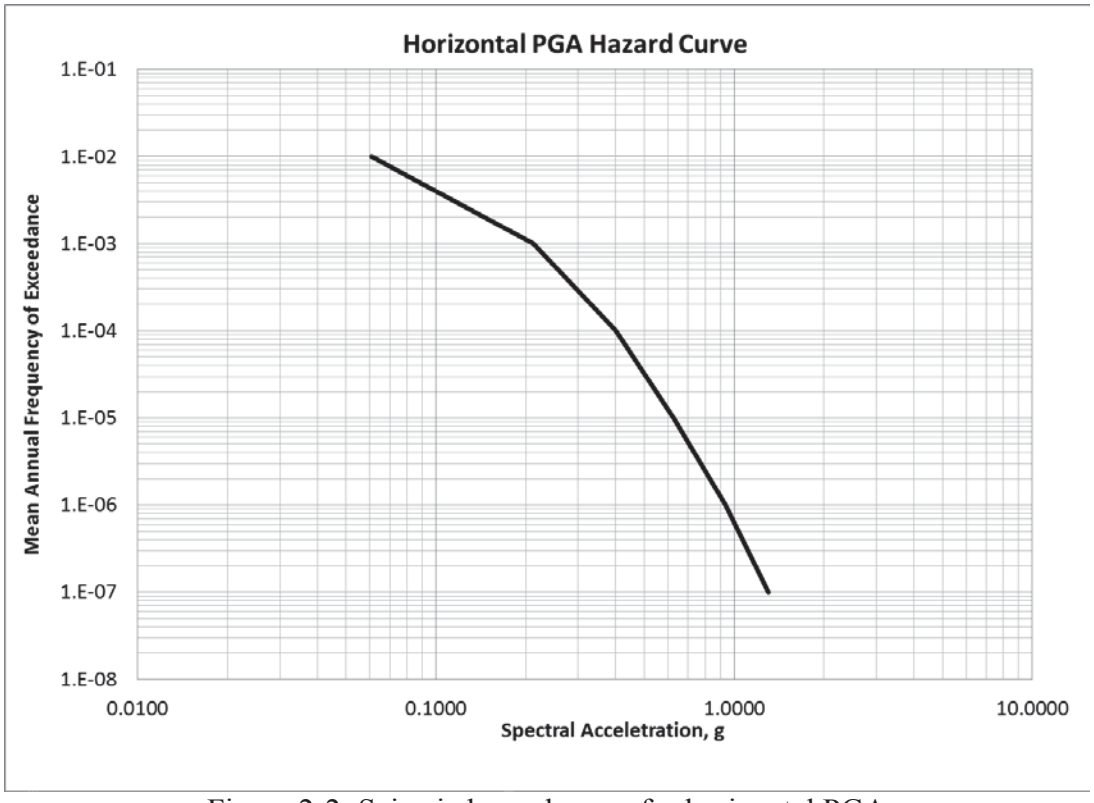

Figure 2-2: Seismic hazard curve for horizontal PGA

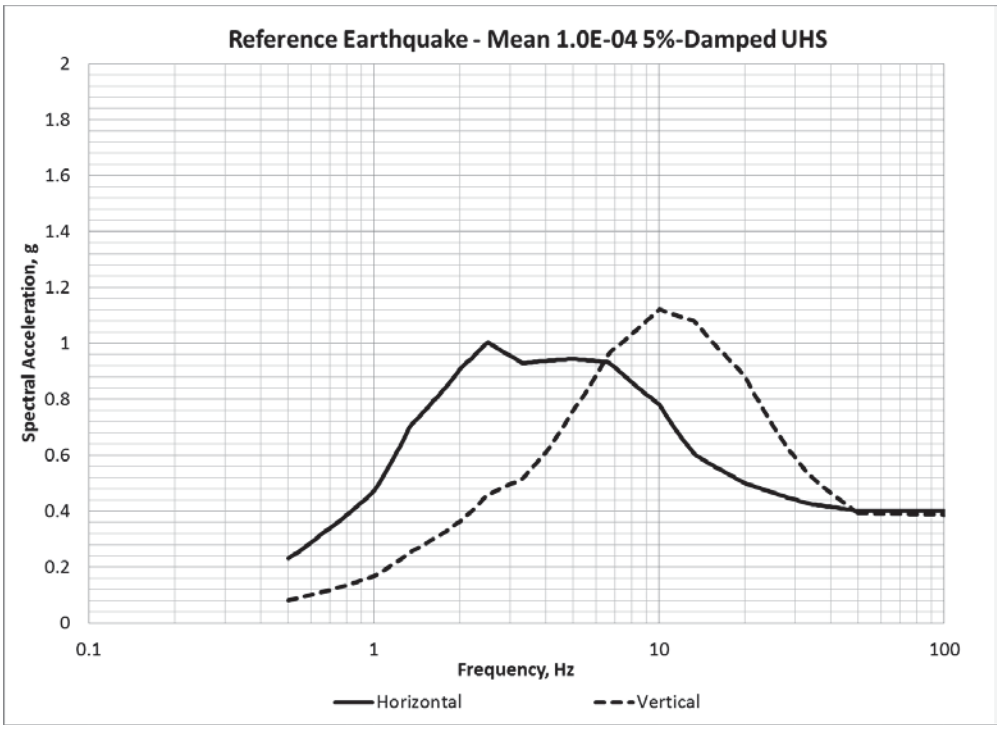

Figure 2-3: UHS for mean annual frequency of exceedance of 1.0E-04

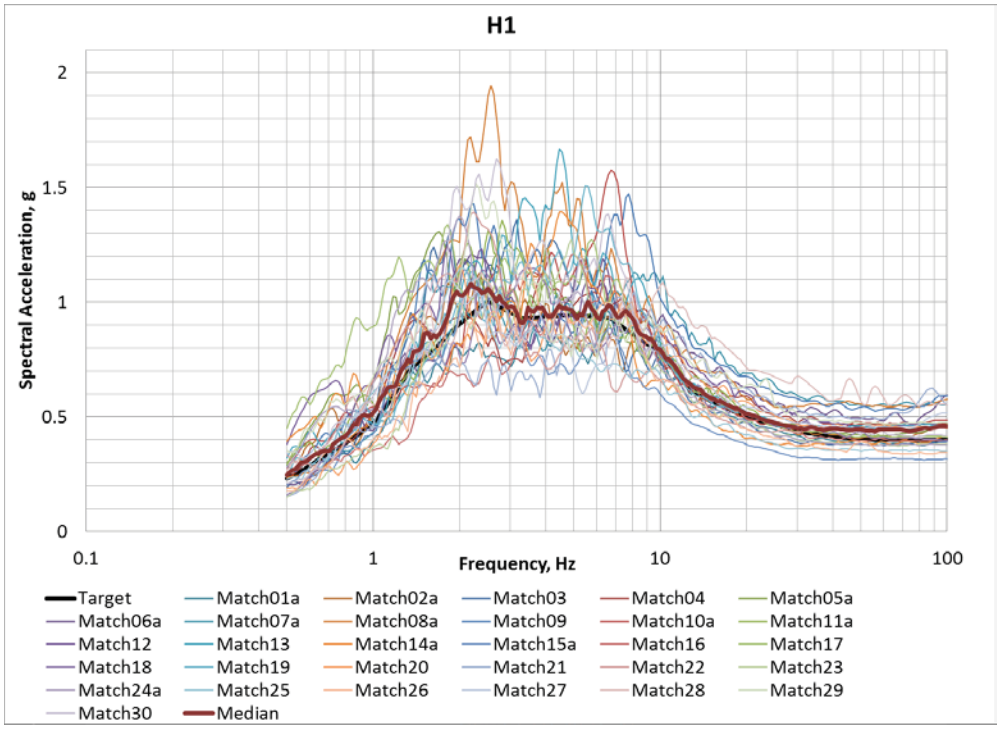

Figure 2-4: Response spectra for reference input ground motions at 5% damping (horizontal component H1)

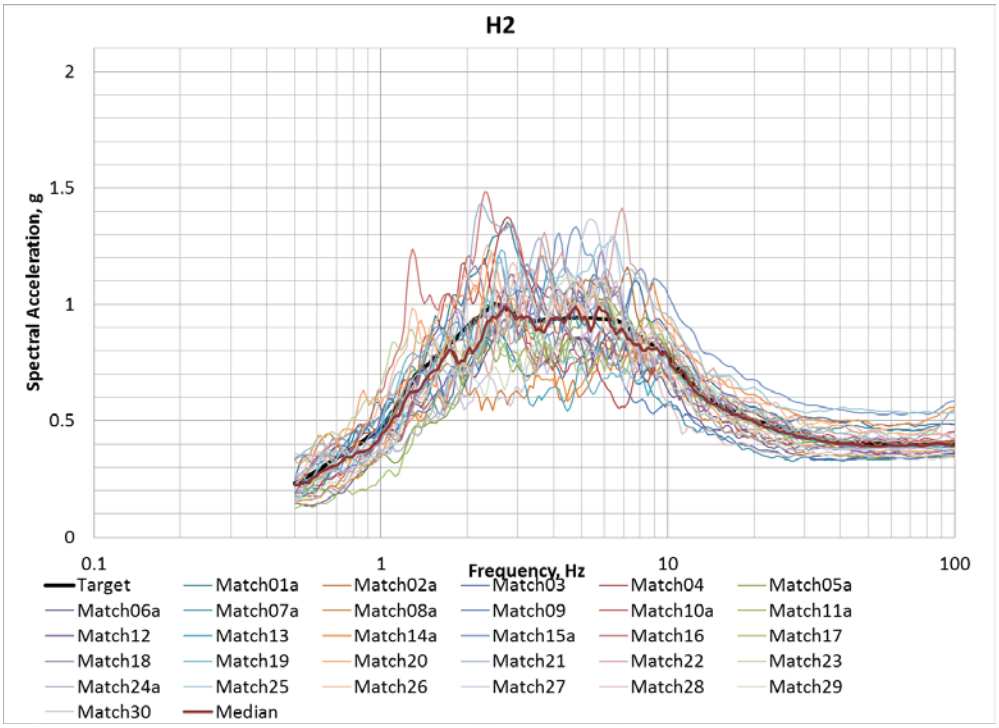

Figure 2-5: Response spectra for reference input ground motions at 5% damping (horizontal component H2)

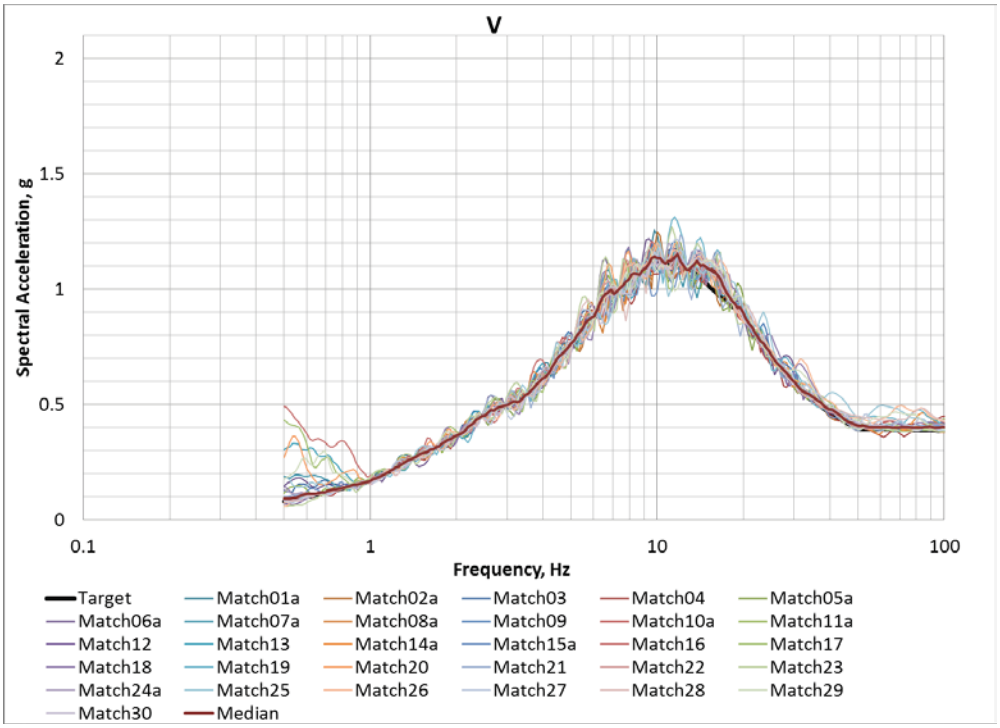

Figure 2-6: Response spectra for reference input ground motions at 5% damping (vertical component V)

2.3 Plant system considered for risk assessment

2.3.1 Equipment Components

The plant system is Emergency Cooling Pump 670-M-11 at the ATR. This pump has an electric motor that is powered by Battery 670-E-58. The motor is started by associated control logic. The system consists of the following components:

- Emergency Cooling Pump 670-M-11 (Figure 3-9)
- Battery 670-E-58 (Figure 3-10)
- Distribution Panel 670-E-23 (Figure 3-11); Circuit Breakers 670-E-23-CB1 and -CB2
- Medium Voltage Switchgear 670-E-1 (Figure 3-12 shows similar Switchgear 670-E-2 with breakers removed); Primary Pump Relay RLY-A

The actual system at ATR also includes Low Voltage Switchgear 670-E-28 and Relay 670-E-28-CR2, Medium Voltage Switchgear 670-E-2 and Primary Pump Relay RLY-A, and Flow Indicator Switch FIS-1-24. These components are excluded from the system model for this study (Section 3.4.3) for simplicity.

Concrete Block Wall 2B-G2-1 is a seismic interaction hazard to Distribution Panel 670-E-23.

The plant system components are all located on the internal structure. Battery 670-E-58 and Medium Voltage Switchgear 670-E-1 are located at Elevation 22ft. The remaining system components are located at Elevation 61ft.

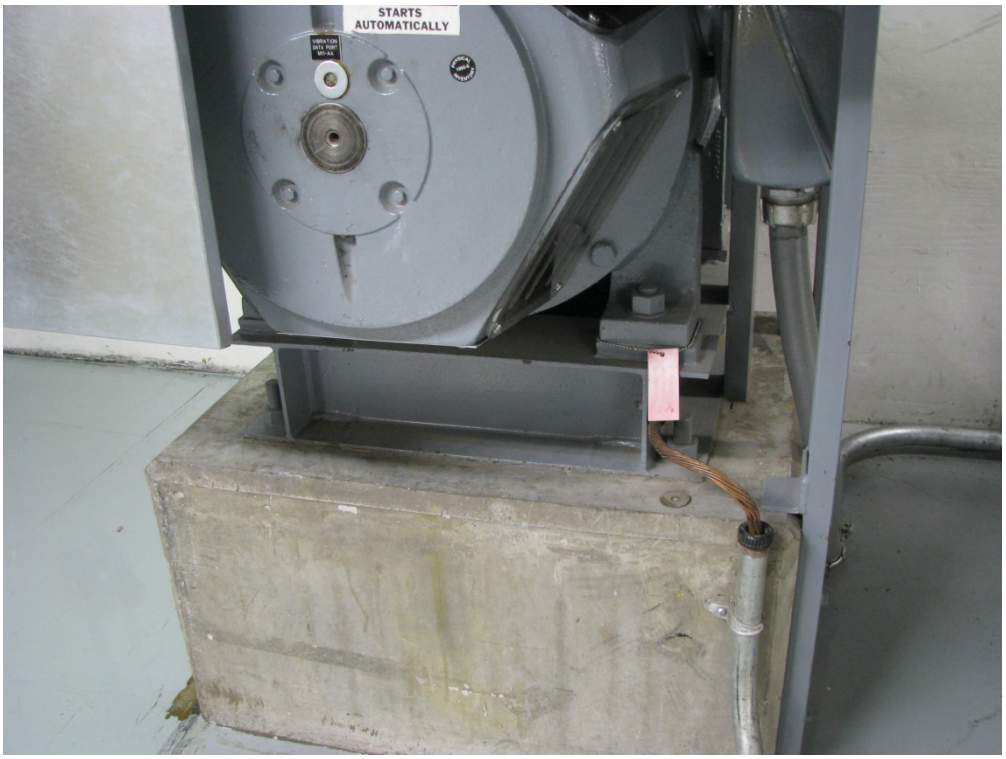

Figure 2-7: Emergency cooling pump 670-M-11

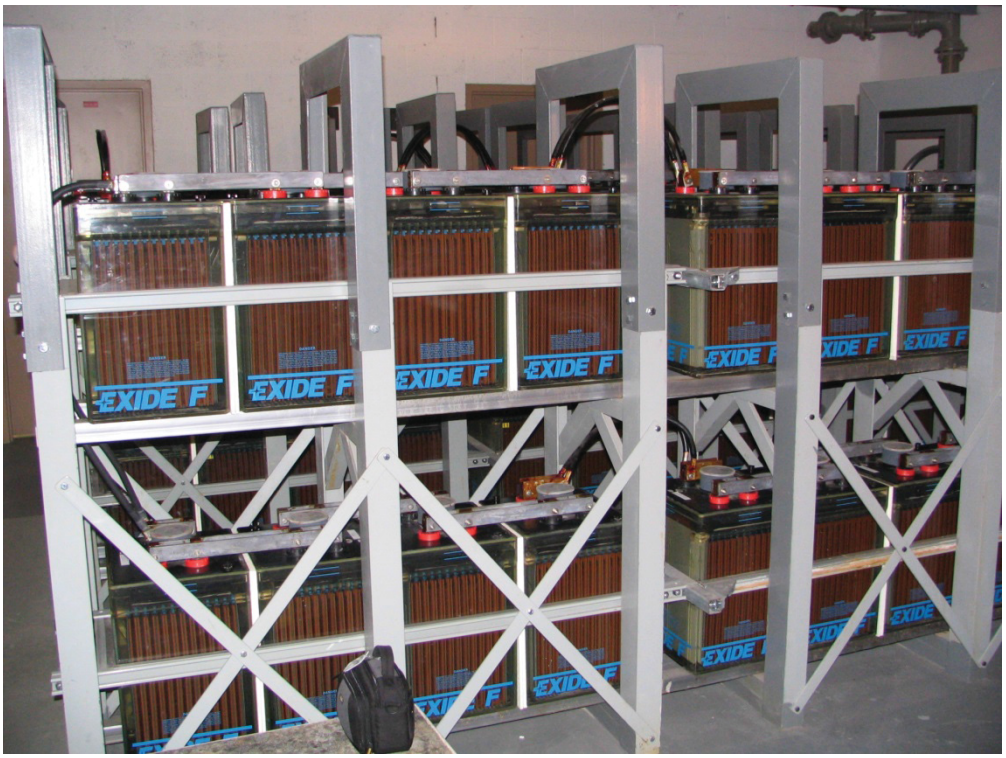

Figure 2-8: Battery 670-E-58

Figure 2-9: Distribution panel 670-E-23

Figure 2-10: Medium voltage switchgear 670-E-2

2.3.2 System Logic Model

Figures 3-13 (a, b, c) show the progressive layers of single-top fault trees for the selected plant system. Figure 3-14 shows the event tree for one earthquake event or intensity level (PDS refers to Plant Damage State). Collapse of Concrete Block Wall 2B-G2-1 will damage Distribution Panel 670-E-23. A sensitivity study will be performed to understand its effect on the plant system risk. INL will calculate the SCDF with and without the block wall.

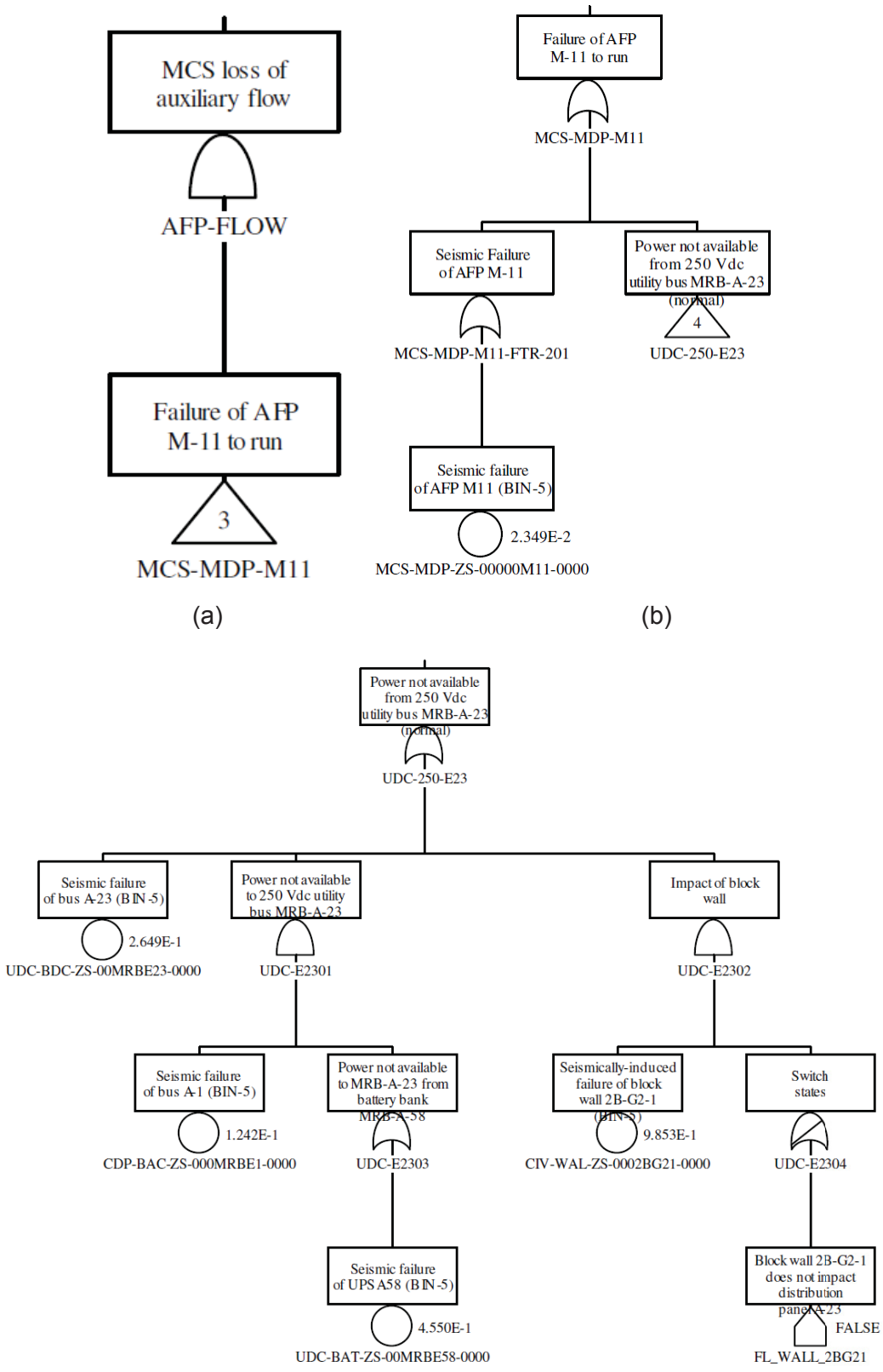

Figure 2-11: System fault trees

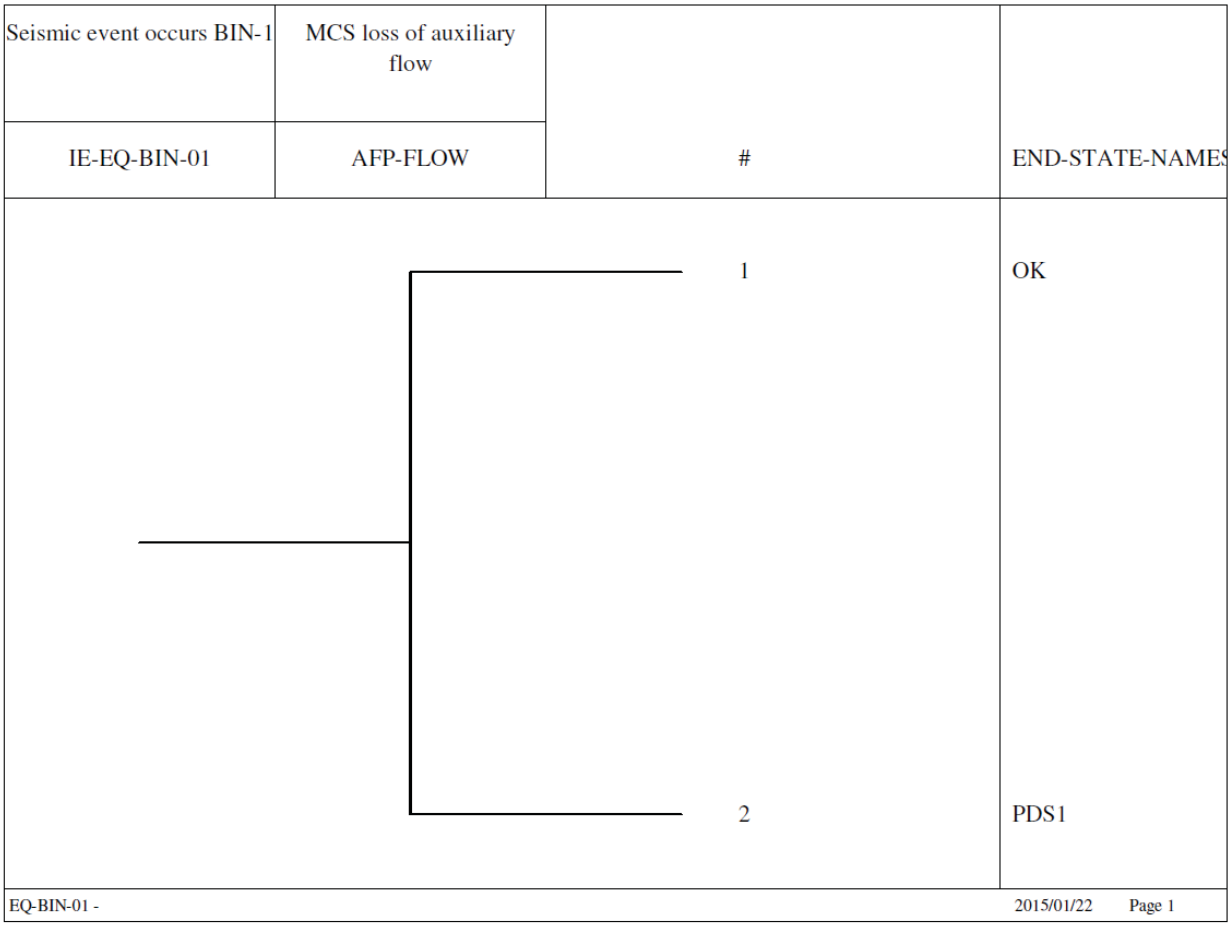

Figure 2-12 – Event tree for earthquake intensity level 1

3. Traditional Seismic Probabilistic Risk Assessment

3.1 Probabilistic seismic response analysis

We performed a probabilistic seismic response analysis of the representative NPP structure using methods typically implemented in a traditional SPRA. Probability distributions for in-structure response spectra (ISRS) at the locations of components of the selected plant system were generated. The analysis consisted of the following steps:

1. Ground motion input consisted of thirty sets of acceleration time histories (Section 3.1).
2. The fixed-base Eigen solution and mass matrix were generated for the structure model with median properties using computer program SAP2000 [2] (Section 3.3).
3. Foundation impedances for the median soil profile under the structure (Section 3.2) were generated using computer program CLASSI [3].
4. Probability distributions of the structure frequency, structure damping, soil stiffness, and soil material damping were represented by scale factors with median values of 1.0 and associated lognormal standard deviations. Representative lognormal standard deviations for structure frequency and damping of 0.15 and 0.35, respectively, were used. Lognormal standard deviations for soil shear modulus and damping of 0.55 and 0.4 were used (Table 3-1).
5. Probabilistic response analysis was performed by the Latin Hypercube Sampling (LHS) approach for thirty simulations using computer program CLASSI. Stratified sampling was used to sample each of the scale factors representing the probability distributions for the variables considered (i.e., structure frequency and damping, soil stiffness and damping, earthquake acceleration time histories). Latin Hypercube experimental design was used to create the combinations of samples for the simulations.
6. Five percent damped median and 84% non-exceedance probability (NEP) ISRS were generated at the component locations. Three and a half percent damped median ISRS were also generated for use in the seismic fragility evaluations.

Table 3-1 lists the randomized property multiplier sets applied to the thirty computer models of the structure and soil. Figures 3-15 through 3-17 show the median and 84% NEP ISRS at Elevation 22ft in the X-, Y-, and Z-directions for 5% damping. Figures 3-18 through 3-20 show the median and 84% NEP ISRS at Elevation 61ft. Median and 84% NEP ISRS for 3.5% damping were also generated.

Table 3-1: Property Randomization Multipliers

Model Number	Structure Frequency	Structure Damping	Soil Shear Modulus	Soil Damping	Soil-Foundation Coefficient of Friction*
1	0.9935	0.6741	1.0412	0.9213	0.75183
2	1.1629	1.5178	1.7367	0.5008	1.15056
3	1.0086	1.0574	1.6487	0.5621	1.01461

Model Number	Structure Frequency	Structure Damping	Soil Shear Modulus	Soil Damping	Soil-Foundation Coefficient of Friction*
4	1.0244	0.5591	0.8781	1.1468	0.94767
5	0.9621	1.1275	0.8498	1.2324	0.87831
6	1.0601	0.4980	1.4524	0.6332	0.82448
7	1.2131	1.3758	1.1158	0.8500	0.84219
8	1.0730	0.9197	0.7247	1.4866	1.03097
9	0.8753	0.7066	1.0092	0.9651	1.17557
10	0.7446	1.3991	0.9720	1.0116	1.24079
11	1.0459	0.7308	2.0275	0.4317	1.13513
12	0.7734	2.2867	0.6451	1.7220	1.09008
13	0.8513	1.0819	1.3094	0.7189	1.2214
14	0.9399	1.2268	1.2243	0.7703	0.87656
15	0.9642	0.9893	0.8116	1.2879	0.92867
16	1.1905	1.3174	0.4520	4.2334	1.46668
17	0.9016	0.7988	1.0889	0.9035	0.80192
18	1.1399	1.7135	1.1820	0.8159	0.72579
19	0.8303	0.9575	0.6308	1.8682	1.35189
20	0.8856	1.1062	0.7680	1.4007	0.78486
21	0.9348	0.8889	0.9220	1.1124	0.91507
22	0.9808	0.9059	1.3733	0.6686	0.99601
23	1.3215	1.6053	0.9365	1.0518	1.73369
24	1.0912	0.6113	0.6938	1.5944	0.5867
25	1.0369	1.1834	3.1721	0.3706	0.68318
26	1.2974	0.7767	0.5751	1.9937	1.31785
27	0.9202	0.8611	1.2611	0.7468	1.04394
28	1.1298	1.2376	0.7917	1.3364	0.96151
29	0.8165	0.8198	1.5447	0.5781	1.06556
30	1.1065	1.0263	0.5107	2.4194	1.41234

* Used in the NLSSI simulations; not used in linear SSI analysis

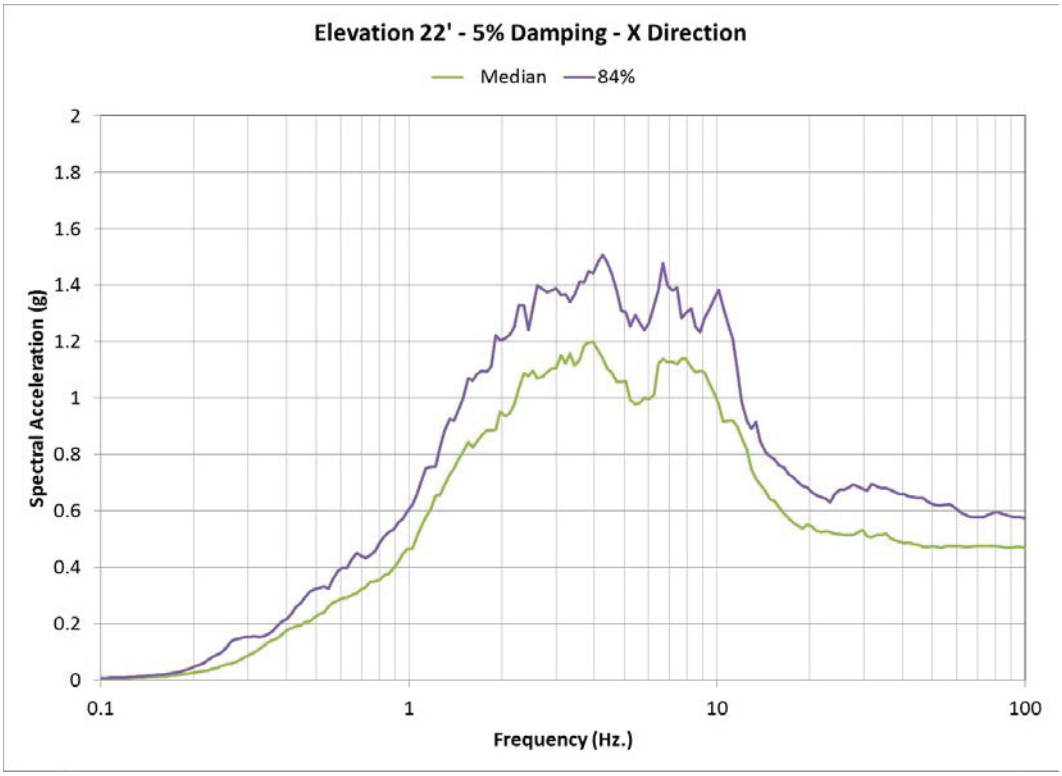

Figure 3-1: Elevation 22ft, X-Direction Response Spectra, 5% Damping

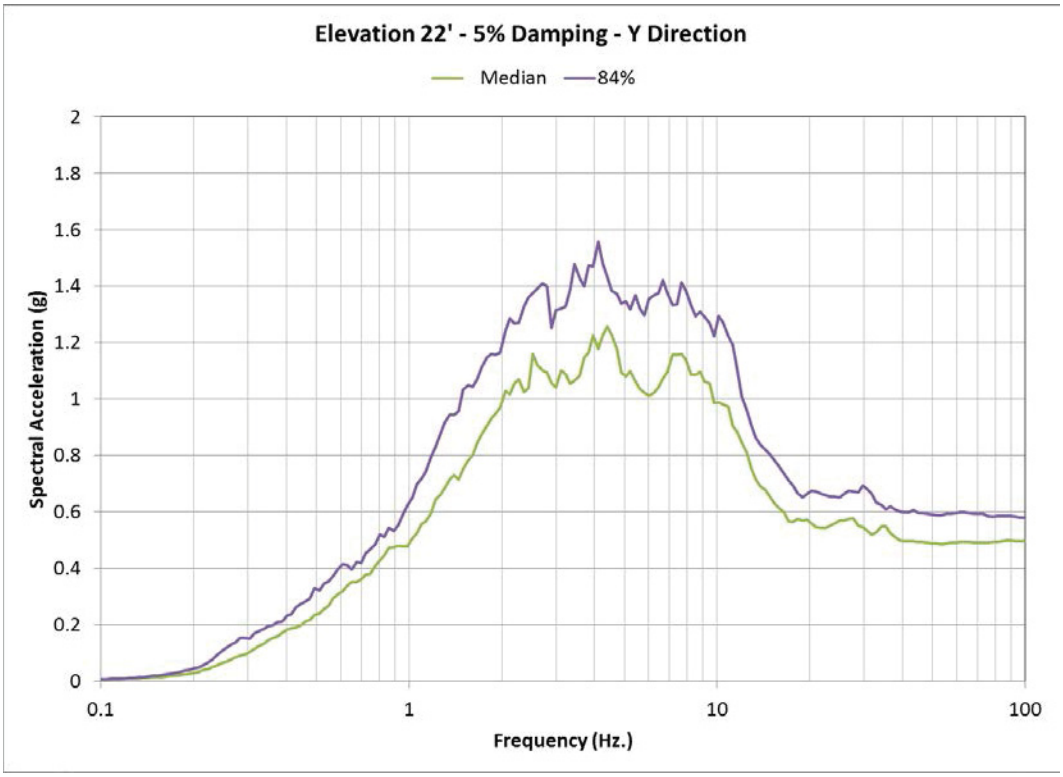

Figure 3-2: Elevation 22ft, Y-Direction Response Spectra, 5% Damping

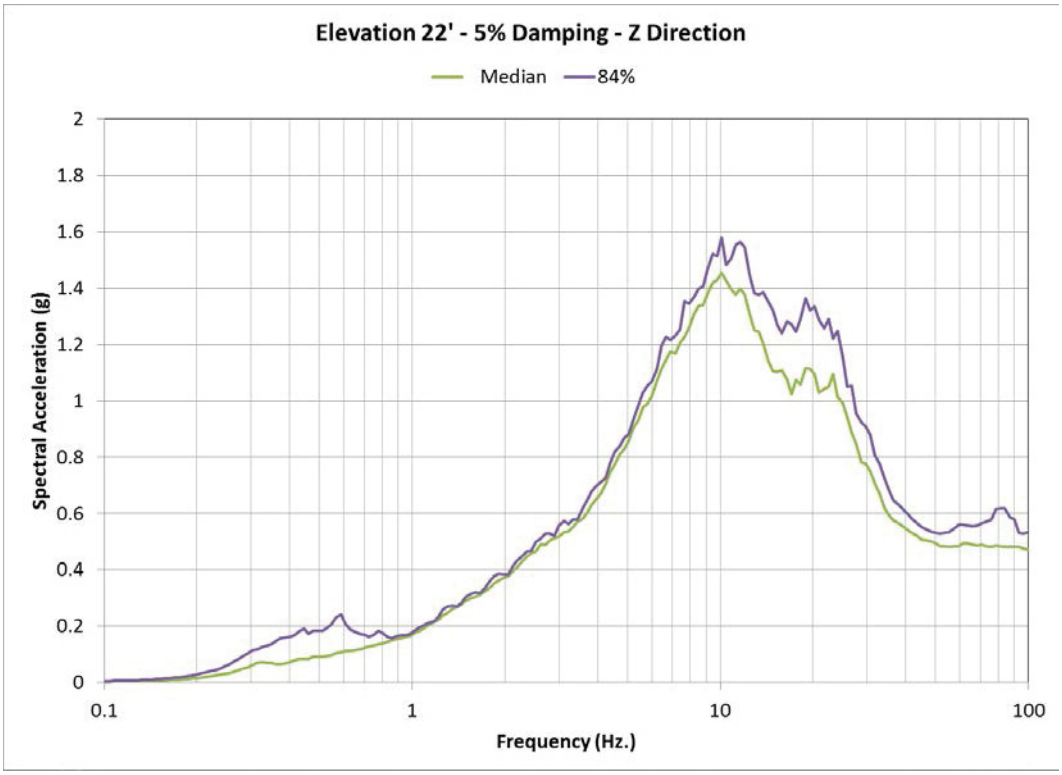

Figure 3-3: Elevation 22ft, Vertical Response Spectra, 5% Damping

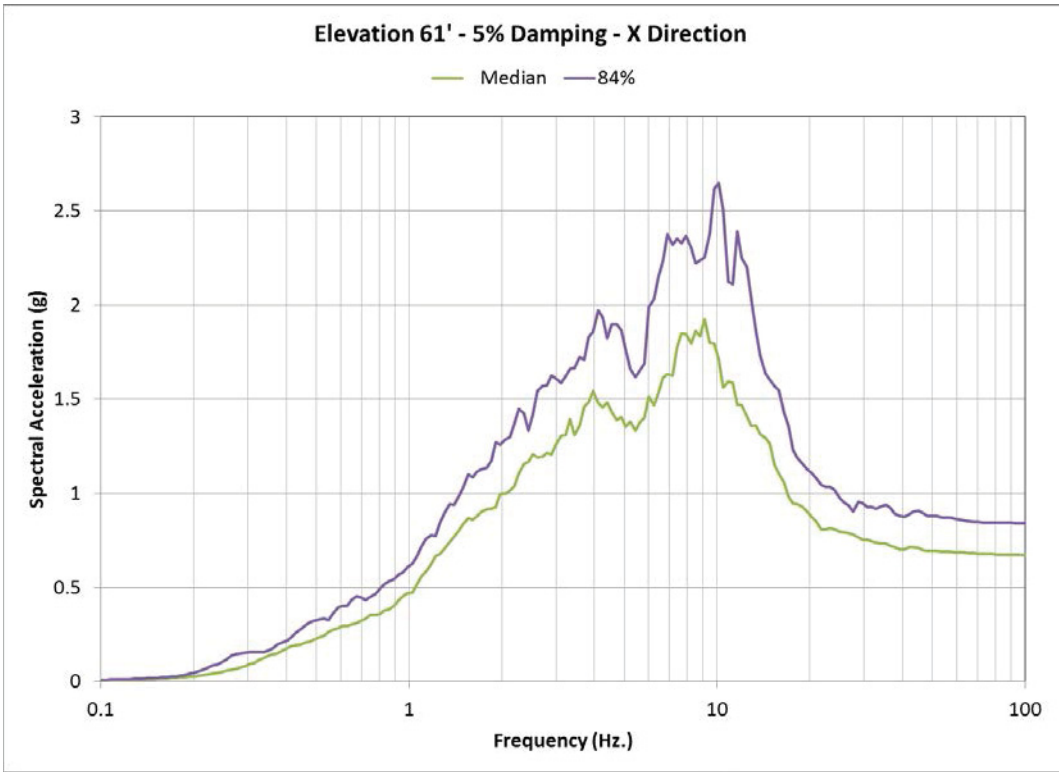

Figure 3-4: Elevation 61ft, X-Direction Response Spectra, 5% Damping

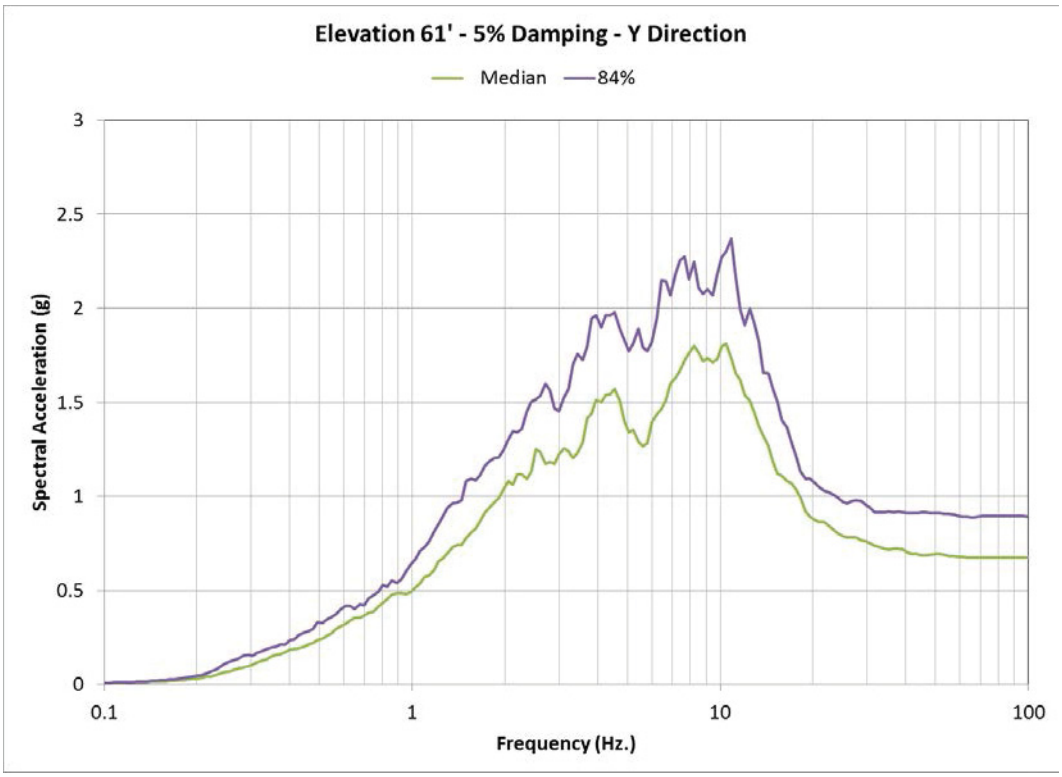

Figure 3-5: Elevation 61ft, Y-Direction Response Spectra, 5% Damping

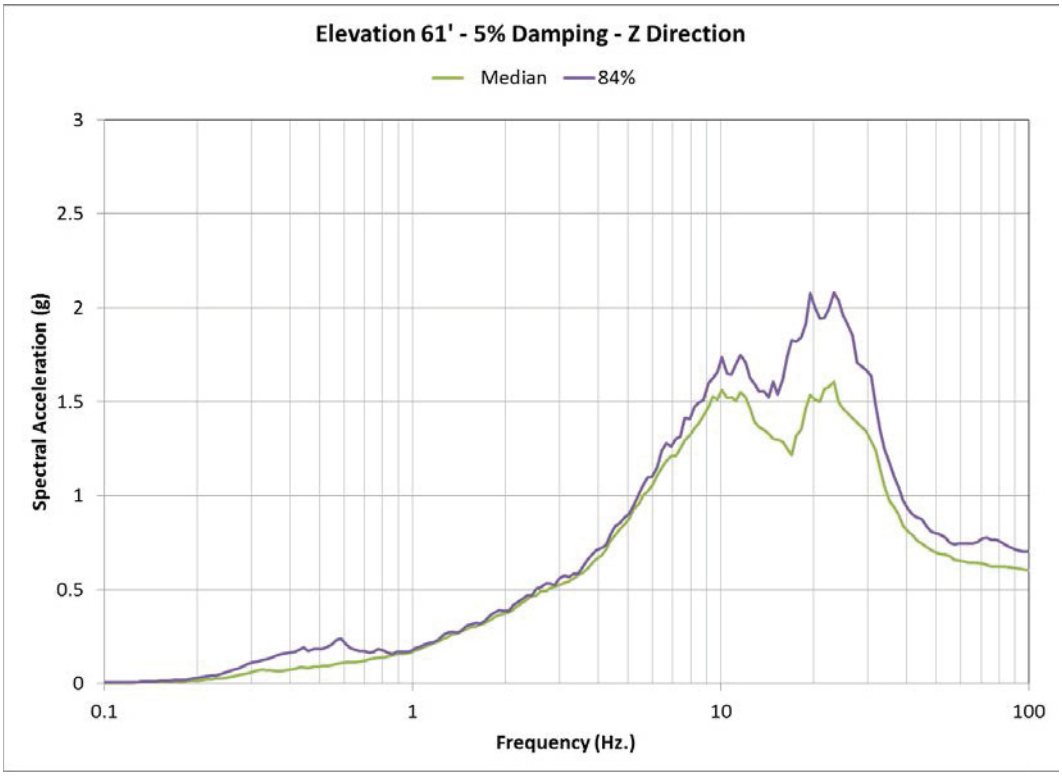

Figure 3-6: Elevation 61ft, Vertical Response Spectra, 5% Damping

3.2 Seismic component fragility evaluation

The system logic model shown in Section 2.3.2 relies on five components of the Emergency Cooling Pump 670-M-11 system. Seismic fragilities for these components are listed in Table 3-2. Their development is summarized below.

Table 3-2: Component seismic fragilities

Component	Floor	A_m	β_c	HCLPF
Pump 670-M-11	EL 61ft	3.40g	0.41	1.31g
Battery 670-E-59	EL 22ft	1.14g	0.28	0.59g
Distribution Panel 670-E-23	EL 61ft	1.60g	0.59	0.40g
Switchgear 670-E-1	EL 22ft	1.90g	0.47	0.64g
Block Wall 2B-G2-1	EL 61ft	0.60g	0.28	0.31g

3.2.1 General approach

The seismic fragilities were calculated by the separation-of-variables method presented in EPRI TR-103959 (Jack R. Benjamin and Associates, Inc. and RPK Structural Mechanics Consulting, 1994) and supplemented by guidance in EPRI 1019200 (Kennedy, et al., 2009). The seismic fragility was expressed as the probability of component failure conditional on the horizontal PGA. The seismic fragility evaluation used existing documentation developed in the previous ATR deterministic seismic evaluation and SPRA, such as DOE/EH-0545 (D.O.E., 1997) Screening and Evaluation Worksheets and screening calculations, and seismic fragility calculations. Component and anchorage configurations were selectively adjusted from the actual configurations to achieve a mix of fragilities controlled by functional and anchorage failure.

Using the separation-of-variables method, the component fragilities were developed in terms of the following factors that contribute to seismic capacity:

- Component capacity: Strength, inelastic energy absorption
- Component response: Qualification method, damping, frequency, mode shape, mode combination, earthquake component combination
- Structure response: Ground motion (including earthquake response spectrum shape, horizontal earthquake peak response, and vertical component response), damping, modeling (including frequency and mode shape), mode combination, time history simulation, and foundation-structure interaction (including ground motion incoherence, vertical spatial variation of ground motion, and SSI analysis)

For this study, variability was represented by the composite lognormal standard deviation without distinction between randomness and uncertainty. Median component capacities, component responses, and associated variabilities were determined on a component-specific basis. Median component responses were determined for the median ISRS obtained by the probabilistic structure seismic response analysis for median component frequencies and

damping. Structure response variability was determined based on the differences between the median and 84% NEP ISRS for the median component frequencies and damping.

Seismic fragility evaluations of the specific components are briefly summarized as follows. Detailed calculations are included in Appendix A.

3.2.2 Emergency cooling pump 670-M-11

Seismic fragility evaluation of Pump 670-M-11 considered only anchorage failure. The pump was considered to be rugged for function. DOE/EH-0545 (D.O.E., 1997) screening of the pump anchorage was documented in Calculation No. 0602301.01-S-113 (ARES Corporation, 2008). The seismic fragility for anchorage failure was obtained by extending the screening calculation.

Pump anchorage consists of smooth L-bolts. The DOE/EH-0545 (D.O.E., 1997) screening evaluation found that anchor bolt tension capacity was limited by pullout. The median pullout capacity was obtained by empirical equations fit to test data from smooth L-bolts. The fragility evaluation determined that anchor bolt tension is controlled by concrete breakout rather than pullout. Median anchor bolt strengths for concrete breakout in tension and shear and associated variabilities were determined using empirical equations that form the basis for current American Concrete Institute anchorage design criteria.

The screening evaluation based pump seismic response on a frequency of 20 Hz. The median frequency may be higher, but the 20 Hz frequency was retained because the NLSSI ISRS at higher frequencies showed artificial numerical response. As a simplification, pump inertial loads for anchorage evaluation were based on the spectral acceleration for 5% damping rather than 3% damping. Differences between the 5% and 3.5% damped in-structure spectral accelerations at 20 Hz are minimal.

3.2.3 Battery 670-E-58

Seismic fragility evaluation of Batteries 670-E-58 and 670-E-59 for the ATR SPRA was documented in SGH Calculation No. 098122-CA-18 (SGH Inc., 2010). In this evaluation, Battery 670-E-59 was found to control over Battery 670-E-58. The existing seismic fragility evaluation of Battery 670-E-59 was consequently adapted to this study and used as a substitute for Battery 670-E-58.

The seismic fragility of the battery set was found to be controlled by failure of the diagonal brace bolts rather than functional failure. The fragility originally calculated for the ATR SPRA was adjusted to the median and 84% NEP ISRS developed for this study (Section 3.5.1).

3.2.4 Distribution panel 670-E-23

The seismic fragility of Distribution Panel 670-E-23 considered anchorage failure. Existing deterministic seismic evaluations were documented in EDF-4316 (INL, 2003) and Calculation No. 0602301.01-S-109 (ARES Corporation, 2008). Adaptation of these calculations to the seismic fragility evaluation included a number of simplifications.

- The back of 670-E-23 is bolted to the side of E-105. Anchorage for E-105 was evaluated for the combined inertia of 670-E-105 and 670-E-23. Anchors for 670-E-23 were considered to be ineffective because they lacked sufficient embedment.

- Anchor bolt shear demands were based on 100-40-40 combination of orthogonal response components rather than SRSS as in EDF-4316 (INL, 2003).
- Anchor bolt compression due to dead weight was included, rather than neglected as in EDF-4316 (INL, 2003).
- Eccentricities due to outriggers connecting 670-E-105 to its anchorage were considered in Calculation No. 0602301.01-S-109 (ARES Corporation, 2008). These eccentricities were disregarded for simplicity.
- Anchor bolts were taken to be 3/4 in. diameter Hilti Kwik-Bolt II, rather than the actual 5/8 in. Kwik-Bolts.
- Calculation No. 0602301.01-S-109 (ARES Corporation, 2008) reduced the capacities of one anchor for 670-E-105 due to its proximity to an anchor for 670-E-103. The capacity reduction for bolt spacing was disregarded for simplicity.

The component horizontal frequency was estimated to be in the range of 5 to 10 Hz. The median frequency was estimated to be 7.5 Hz, and a frequency of 5 Hz was judged to have a 10% NEP. Median component damping was estimated to be 5%. Median seismic response was based on the median 5% damped in-structure spectral acceleration at the median frequency.

The median anchor bolt tension and shear strengths were based on mean values listed Table 2.6 of EPRI NP-5228-SL, Volume 1 (EPRI, 1991). Tension-shear interaction equations in EPRI TR-103959 (Jack R. Benjamin and Associates, Inc. and RPK Structural Mechanics Consulting, 1994) were implemented.

3.2.5 Medium voltage switchgear 670-E-1

Experience-based seismic evaluation of Switchgear 670-E-1 by DOE/EH-0545 (D.O.E., 1997) procedures found that it satisfied the screening caveats, but its anchorage and Primary Pump Relay RLY-A did not. As a simplification for this study, the switchgear seismic fragility was developed for functional failure, and anchorage and relay failure were excluded.

Because the switchgear effectively satisfies the EPRI NP-6041-SL (EPRI, 1991) screening criteria for a 1.2g ground spectral acceleration, the median in-structure spectral acceleration capacity was determined to be 4.8g based on EPRI 1019200 (Kennedy, et al., 2009). The switchgear frequency was estimated to be in the range of 5 to 10 Hz. Following EPRI TR-103959 (Jack R. Benjamin and Associates, Inc. and RPK Structural Mechanics Consulting, 1994), narrow spectral peaks may be clipped to obtain equivalent broadband spectral demand for comparison to broadband spectral capacity. The clipped spectral acceleration was judged to be no less than the valley of the ISRS at 6.0 Hz.

3.2.6 Concrete block wall 2B-G2-1

Collapse of Concrete Block Wall 2B-G2-1 is a seismic interaction hazard to Distribution Panel 670-E-23. This wall was evaluated as part of Wall Group 1 in Calculation No. 0602301.01-S-007 (ARES Corporation, 2008). The block wall seismic fragility was developed by extending the Conservative Deterministic Failure Margins Method in Appendix R of EPRI NP-6041-SL (EPRI, 1991) to the determination of a median collapse capacity.

4. Advanced Seismic Probabilistic Risk Assessment using Nonlinear Soil-Structure Interaction Analysis

4.1 Introduction

Nonlinear soil-structure interaction (SSI) analysis in this section is performed using the commercial time-domain code, LS-DYNA. LS-DYNA is a commercial finite-element program, currently developed and maintained by the Livermore Software Technology Corporation (LSTC). It is predominantly used for solving structural mechanics problems using the explicit integration algorithm, which makes it suitable for applications involving sudden loads (crash and blast simulations) and contact problems. The implicit integration algorithm is also implemented in LS-DYNA, but with limited capabilities. LS-DYNA includes a large database of material models for simulating soil and structure (especially steel and concrete), contact interfaces and seismic isolators. LS-DYNA has seen increasing usage in the civil engineering industry with applications in nonlinear site-response, and soil-structure interaction (SSI) analyses of buildings, bridges and LNG tanks (Willford *et al.*, 2010). LS-DYNA is therefore considered a suitable choice for nonlinear SSI analysis of this study.

Nonlinear response in SSI analyses is a result of 1) nonlinear site response, which affects the foundation-level input motion to the structure, 2) hysteretic response of the soil at the vicinity of the foundation, which results in foundation flexibility and hysteretic energy dissipation at the foundation and 3) gapping and sliding of the foundation. The nonlinear SSI analyses in this report are performed considering only the geometric nonlinearities at the foundation-soil interface, which are of primary interest in this study. In-structure response spectra (ISRS) at the locations of selected components are calculated and used in the seismic fragility calculations. The seismic fragilities for each component are then compared with those calculated using the traditional SPRA process described in Section 3.

4.2 Nonlinear SSI modeling

4.2.1 The NLSSI methodology

Spears and Coleman (2014) proposed methodology to perform nonlinear soil-structure interaction analysis in the time domain. This methodology, referred to as the NLSSI methodology, is a series of steps that an analyst of reviewer can follow to perform a fully nonlinear SSI analysis in the time domain including 1) nonlinear site response, 2) nonlinear hysteretic soil behavior at the foundation vicinity, 3) geometric nonlinearities at the foundation including gapping and sliding and 4) nonlinear behavior of the structure such as concrete cracking. The NLSSI methodology is illustrated in the flowchart presented in Figure 4-1 and is used to perform the nonlinear SSI analyses in this project. As shown in the flowchart, building an NLSSI model involves 1) building the structural model, 2) building the soil domain model, 3) building the interface model and 4) specifying the input. Each of these models should be independently verified for the desired properties before assembling the NLSSI model and performing the analysis to calculate the output.

The nonlinear SSI analyses of this study are performed along the lines of the NLSSI methodology. The description of structural modeling, soil domain modeling and input specification, interface modeling, and the NLSSI model assembly are presented in Sections

4.2.2, 0, 4.2.4 and 4.2.5, respectively. Verification and/or benchmarking are performed for each of the individual models as explained in the corresponding sections.

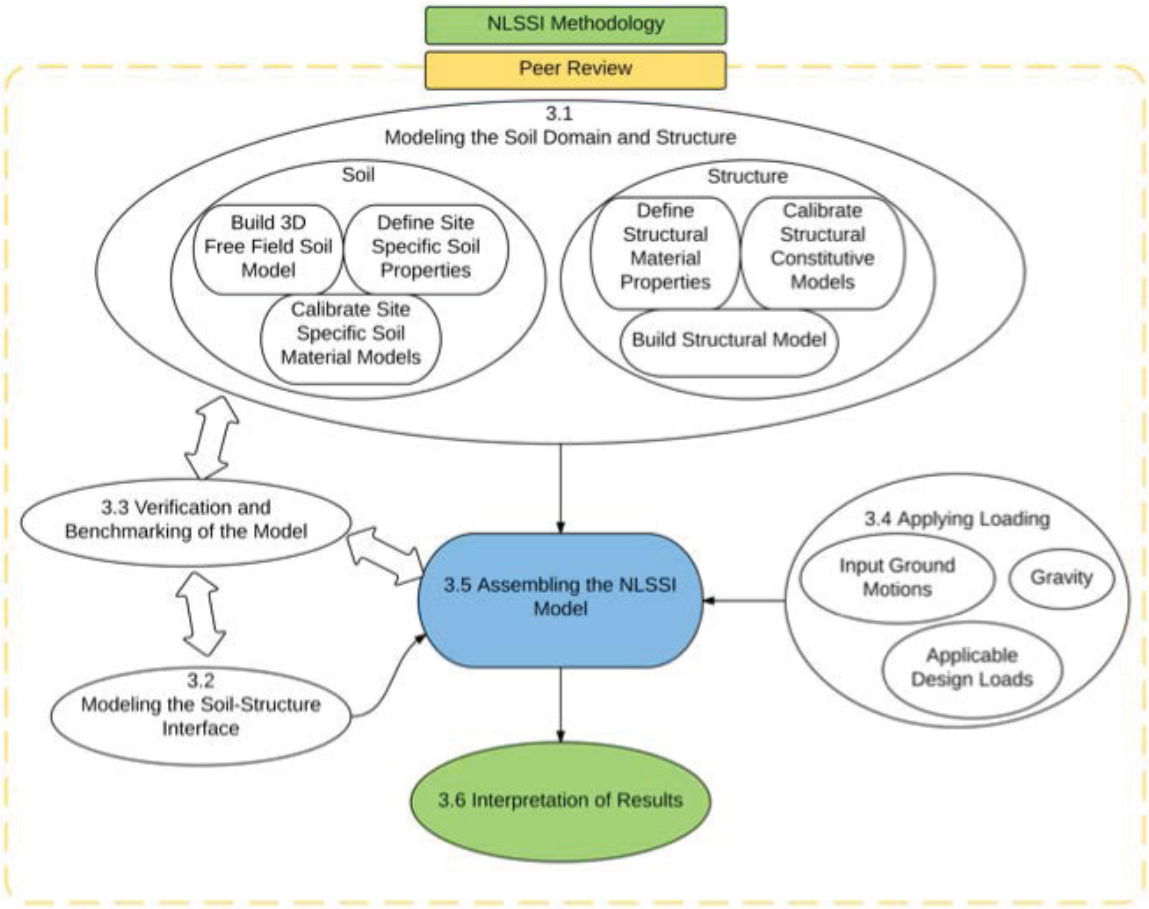

Figure 4-1: The NLSSI methodology (Coleman *et al.*, 2015)

4.2.2 Structural modeling

4.2.2.1 Modal Analysis

The LS-DYNA model of the representative NPP structure is built using the Belytschko-Schwer resultant beam elements (beam element type 2) and assigning the cross-section properties presented in Figure 2-1. Note that assigning a zero mass density is not possible in LS-DYNA (unlike in CLASSI and SASSI) and a small value of 10^{-4} kip-sec^2/ft^4 (actual mass density of concrete is 0.0047 kip-sec^2/ft^4) is used instead. A fixed-base, modal analysis is performed for the representative NPP structure and the modal frequencies, mass participations and mode shapes of the first 15 modes are calculated. The modal frequencies are presented in Table 4-1 below, along with the frequencies calculated by SGH using the structural analysis code, SAP2000 (Computers and Structures Inc., 2011). The modal frequencies calculated using SAP2000 and LS-DYNA are clearly identical. The mass participations, and mode shapes (not presented here) calculated using the two programs are also almost identical.

Table 4-1: Modal frequencies of the representative NPP structure calculated using SAP2000 and LS-DYNA

Mode	Modal Frequency (Hz)	
	CLASSI/ SAP2000	LS-DYNA
1, 2	5.27	5.26
3, 4	8.46	8.45
5, 6	12.37	12.37
7	15.64	15.64
8, 9	16.24	16.24
10	27.83	27.83
13, 14	32.89	32.89

4.2.2.2 Fixed-base response-history analysis

After verifying the modal frequencies, a fixed-base response-history analysis (RHA) is performed with one set of acceleration inputs (three components), and the LS-DYNA responses at key locations in the NPP structure are compared with those calculated by SGH using CLASSI. The stick model used for modal analysis is also used for the RHA. Input ground motions are applied at the base of the structure as prescribed accelerations, and a Rayleigh damping of 5% (median damping ratio of the structure) is specified in the frequency range of 5Hz to 35Hz. Rayleigh damping is modeled in LS-DYNA by specifying the mass damping coefficient using the *DAMPING_PART_MASS card, and the stiffness damping coefficient using *DAMPING_PART_STIFFNESS card. The mass and stiffness damping coefficients are calculated through a trial-and-error procedure to achieve roughly 5% damping in the frequency range specified above.

Since LS-DYNA employs an explicit integration algorithm for RHA, it requires that the analysis time step be less than a critical time step. The critical time step of a model is governed by its stiffness element (beam, solid, shell or any other element) and is equal to the duration of propagation of a wave through this element (Bathe, 1996; LSTC, 2009). In the case of beam elements, the critical time step is directly proportional to the square root of the mass density of the beam material. For this reason, a small value of mass density (e.g., 10^{-4} kip-sec^2/ft^4 used for modal analysis) can drastically reduce the critical time step and increase the computation time. In order to avoid large computation times in the RHA, the beam material density is increased to 0.0047 kip-sec^2/ft^4, which is equal to the actual material density of concrete. The lumped masses at the nodes are then adjusted compensate for the increased mass density of the beams, assuming that the mass of each beam is equally lumped to the two beam nodes. Sample results of the RHA performed using this approach are presented in Figure 4-2 below. The results present the 5% damped acceleration response spectra of the internal structure at an elevation of 22ft in the X direction. Figure 4-2 shows that the structural responses calculated using CLASSI and LS-DYNA are very different, in spite of the models using identical properties and having identical

modal frequencies. Further investigation into these differences revealed some issues with modeling in LS-DYNA as described below.

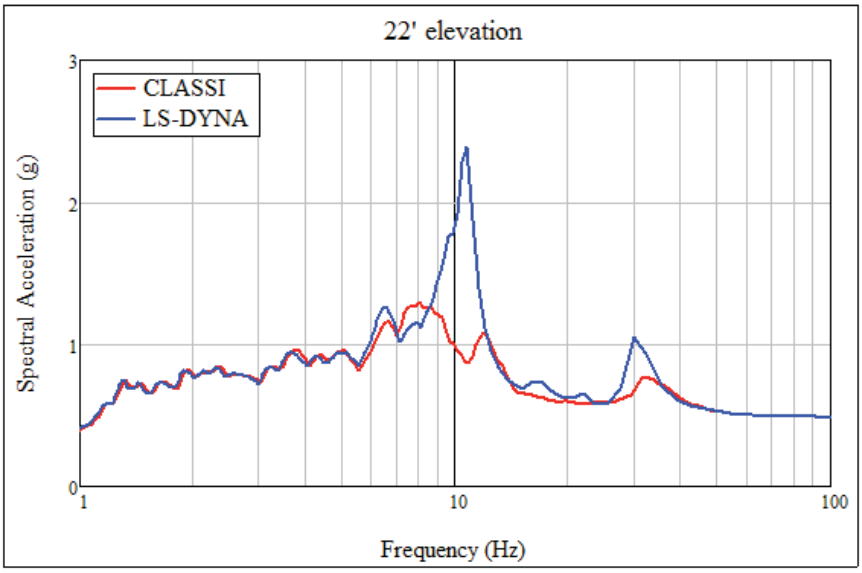

Figure 4-2: Spectral acceleration in the internal structure at 22ft elevation calculated using CLASSI and a preliminary model in LS-DYNA

4.2.2.3 Practical issues faced

Figure 4-2 shows that the response spectrum calculated from the LS-DYNA results differs from that calculated using CLASSI in two aspects: 1) the peak spectral acceleration calculated using LS-DYNA is significantly higher and 2) the frequency of this peak spectral acceleration (about 11 Hz) is considerably higher. These differences indicate that the damping in LS-DYNA is not accurately simulated, and that the natural frequencies of the RHA model do not match with those calculated in the modal analysis (1st mode frequency of the internal structure is about 8.5Hz; see Table 4-1). After a detailed investigation that included performing element level analyses in LS-DYNA, performing SASSI (Lysmer *et al.*, 1999) analyses, and consultations with other LS-DYNA users (Robert Spears, Personal Communication, 2015) and the LS-DYNA technical support (Ushnish Basu, Personal Communication, 2015), the following errors were recovered from the preliminary LS-DYNA model and fixed:

1. Modeling Rayleigh damping: Rayleigh damping in LS-DYNA is modeled by specifying the mass damping coefficient, α, and the stiffness damping coefficient, β, using the *DAMPING_PART_MASS and *DAMPING_PART_STIFFNESS cards, respectively. The mass damping coefficient is specified as a load curve, LCID, (LSTC, 2013) and a scale factor, SF. The ordinate of LCID denotes the time, namely, LCID stands for mass damping coefficient vs. time. Since no description of LCID was provided in the LS-DYNA manual, the ordinate of LCID was assumed to be the part number in the preliminary analysis. It was also found that the mass damping is not applied to nodal masses that are modeled using *ELEMENT_MASS, explaining the significantly larger spectral accelerations. Additionally, although unclear from the manual, it was found that the stiffness damping, β, should be

specified as a negative number, in order to accurately model Rayleigh damping. The preliminary analysis was performed using a positive number for β, which simulates a different kind of stiffness damping that is different from the Rayleigh damping coefficient.

2. Mass distribution in beam type 2 (Belystschko-Schwer resultant beam): Most finite-element structural analysis programs use a lumped-mass matrix for beam elements that distribute the mass of the beam equally to the two beam nodes. This assumption was used to update the lumped masses in the preliminary model to compensate the non-zero beam material density. However, after performing some element-level analyses, it was found that the type 2 resultant beam also lumps the rotational inertia from the beam mass on to the nodes of the beam element, causing the change in the natural frequencies. Since the expression for this lumped rotational inertia is not known, a similar model cannot be created in CLASSI, making it almost impossible to maintain equivalence between the structural models. Facing this conundrum, it was decided that a very small density be used for the beam material (which reduced the rotational inertias to almost zero), along with the lumped masses used in CLASSI/SAP2000. In order to avoid the exceptionally large computation time, which is a consequence of the small density, the time step of the analysis was artificially increased to 10 times the critical time step. Given that this increase may result in numerical instabilities, each RHA is monitored by comparing the results with those calculated from CLASSI, and by examining the energy balance in the model.

The preliminary structural model in LS-DYNA was updated to counter the issues described above. Fixed-base analyses were also performed in SASSI for further verification. Results from the updated model are presented in Figure 4-3, which also includes the CLASSI and SASSI responses. The figure shows that the CLASSI, SASSI and updated LS-DYNA models result in very similar responses, hence proving the equivalence of the structural models.

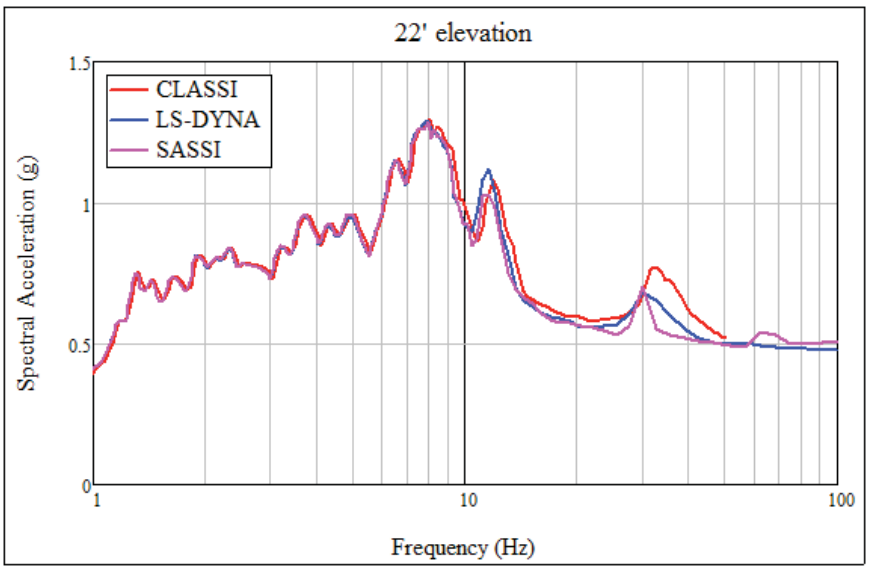

Figure 4-3: Spectral acceleration in the internal structure at 22ft elevation calculated using CLASSI, SASSI and the updated model in LS-DYNA

4.2.2.4 Results of fixed-base response-history analyses

After verifying that the CLASSI and LS-DYNA models are equivalent, a fixed-base analysis is performed with the updated LS-DYNA model with simultaneous ground motion input in the X, Y and Z directions. The results of this analysis (spectral accelerations in the internal structure at 22ft and 61ft elevations) are presented in Figure 4-4. The figure includes the results calculated using 1) CLASSI, 2) updated LS-DYNA model with the default time step (referred to as 'LS-DYNA' in the legend), and 3) updated LS-DYNA model with scaled time step (referred to as 'LS-DYNA tstep' in the legend).

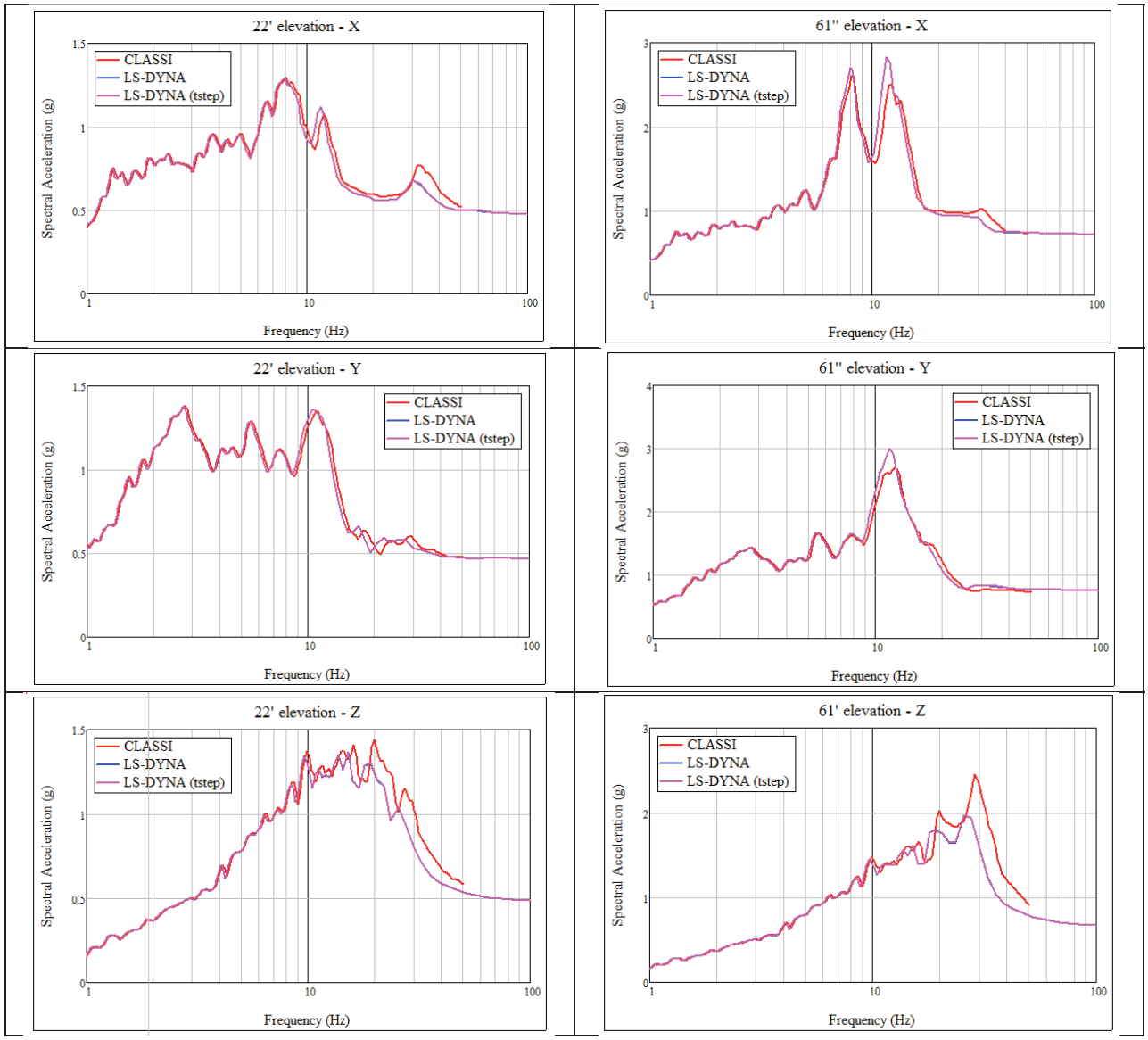

Figure 4-4: 5% damped spectral accelerations of the internal structure at 22ft elevation (left) and 61ft elevation (right)

Figure 4-4shows that the CLASSI and LS-DYNA responses are almost identical in the X and Y directions. Small differences exist between the responses in the Z direction, with LS-DYNA predicting smaller spectral accelerations at the higher frequencies. This might be due to the

differences in the damping formulations: the CLASSI model uses a frequency-independent damping formulation, while the LS-DYNA model uses Rayleigh damping. The figure also shows that the results of the LS-DYNA analysis with a (10 times) scaled time step are identical to those calculated with the default time step. Therefore the scale factor of 10 for the time step is considered suitable for fixed-base analyses with other ground motion inputs.

4.2.3 Soil domain modeling and specification of ground motion input

Soil-structure interaction in the time domain is typically performed using the direct method (Bolisetti and Whittaker, 2015; Spears and Coleman, 2014). In the direct method, the whole soil-structure system is analyzed in a single step thereby circumventing the use of superposition, which is extensively used in traditional SSI analysis methods (including SASSI and CLASSI) and is restricted to linear analyses. This enables a more realistic simulation with the use of nonlinear material models for the soil and structure, and contact models that simulate separation and sliding at the foundation-soil interface. Soil-structure interaction analysis using the direct method can be performed using most commercial finite-element codes such as ABAQUS (Dassault Systèmes, 2005), ANSYS (ANSYS Inc., 2013), LS-DYNA, or the open source finite-element code, OpenSees (Mazzoni *et al.*, 2009). Figure 4-5 presents a sample finite-element model for SSI analysis using the direct method in LS-DYNA.

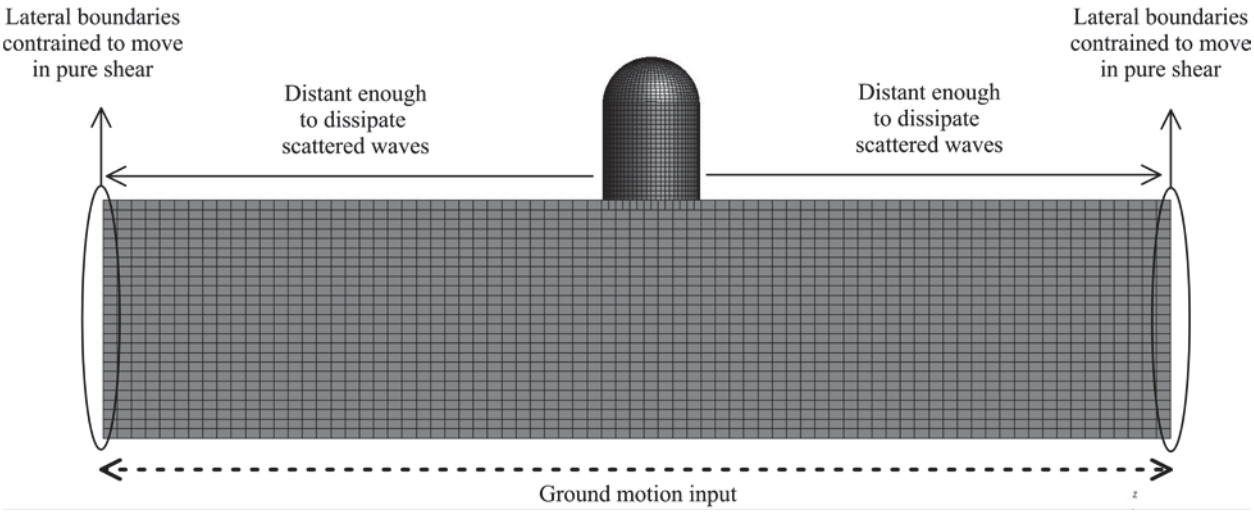

Figure 4-5: Description of a finite-element model for soil-structure interaction analysis using the direct method (Bolisetti *et al.*, 2015)

The finite domain in the direct method needs to satisfy the following conditions in order to simulate an infinite domain: 1) effective damping of the waves radiating away from the structure so that they do not reflect back into the soil domain from the lateral boundaries, and 2) stress equilibrium at the lateral boundaries to account for the rest of the soil domain that is not included in the finite domain model. The former is achieved by building a large soil domain with sufficient plan dimensions to dissipate the radiating waves before they reach the lateral boundaries. In this approach, the radiating waves are dissipated through hysteresis and viscous damping in the soil. The plan dimensions of the domain can be determined by a trial-and-error procedure, ensuring that the acceleration responses at the boundaries of the soil domain are equal

to the free-field acceleration, which is calculated from a separate site-response analysis, and also by verifying that the structural response does not change with a further increase in the domain size. Stress equilibrium at the lateral boundaries can be obtained by constraining the boundary nodes at each elevation to move together in each direction. This enables the elements at the boundaries to move in pure shear, thus simulating a free-field condition (assuming that the input comprises vertically propagating shear waves), as shown in Figure 4-5.

The LS-DYNA numerical model for the SSI analysis of the representative NPP structure is presented in Figure 4-6. As illustrated in the figure, the soil domain of this model is 665ft × 665ft in plan (about 5 times the size of the basemat, which is 131ft in diameter), and 214ft deep. The dimensions of the soil domain are chosen after trying two soil domain sizes. The chosen dimensions are verified by comparing the surface response at the edge of the soil domain to the free-field response from a separate one-dimensional site-response analysis. The soil domain is built with about 192,000 solid elements that have an almost uniform size of 8ft in all directions. This element size allows the propagation of frequencies up to about 40Hz, assuming 10 elements per wavelength. The base of the soil domain is modeled as a transmitting boundary using the *BOUNDARY_NON_REFLECTING option in LS-DYNA. The ground motion input in the CLASSI analysis is applied at the free field, which is not possible in the direct method. However given that soil domain is completely uniform, it can be assumed that the ground motion recorded at the free field is caused purely by the incident waves from the soil domain. These incident waves can be applied as an outcrop input to the LS-DYNA soil domain at any depth, in order to achieve the same free-field ground motion as CLASSI. The outcrop input is applied as a shear force history as shown in Figure 4-7. This creates an incident wave that is reflected back into the soil domain at the surface. The dampers shown in Figure 4-7 absorb the reflected wave, simulating an infinite soil domain. To verify that the input excitation in CLASSI and LS-DYNA are equivalent, the free-field response from LS-DYNA (which is the surface response of the soil at the edge of the domain far from the structure) is compared with the free-field input in the CLASSI simulations. Figure 4-8 presents the spectral accelerations of the free-field input in CLASSI and the free-field response in LS-DYNA in X, Y and Z directions. The figure clearly shows that the responses are almost similar, except that the LS-DYNA response is slightly smaller in the higher frequencies. This can be attributed to 1) finite domain effects and 2) difference in the damping formulations in the two codes.

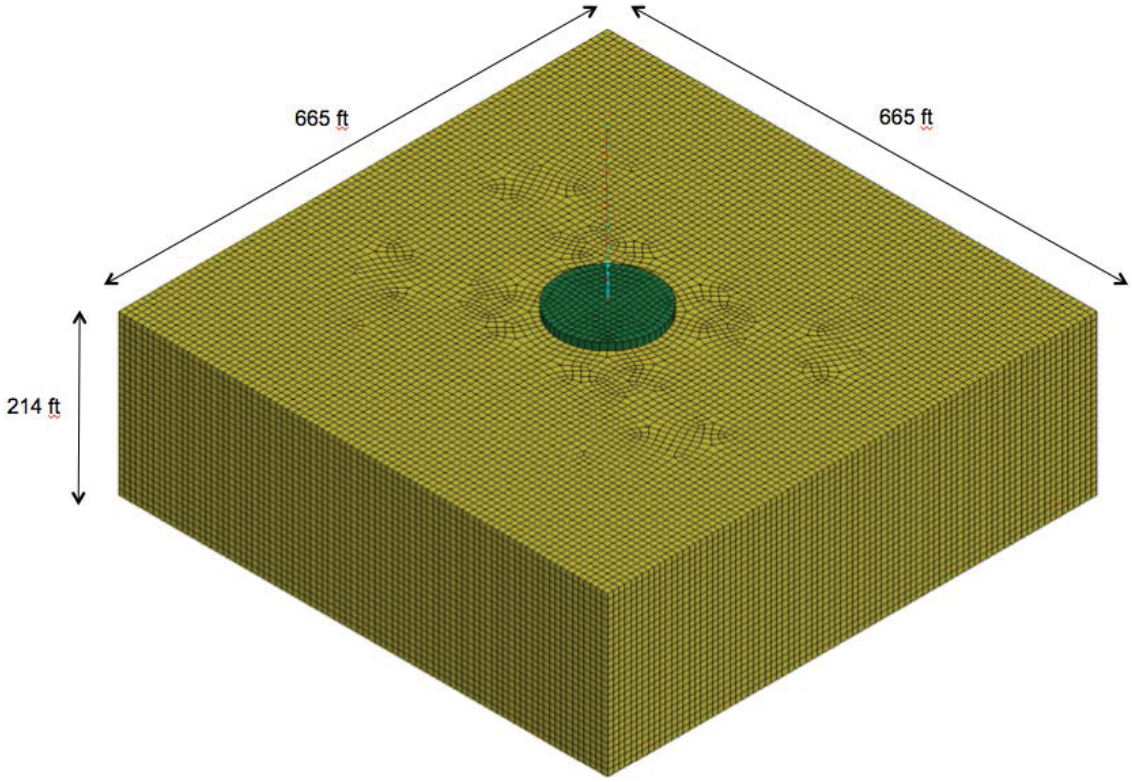

Figure 4-6: Finite-element model for the SSI analysis of the representative NPP structure

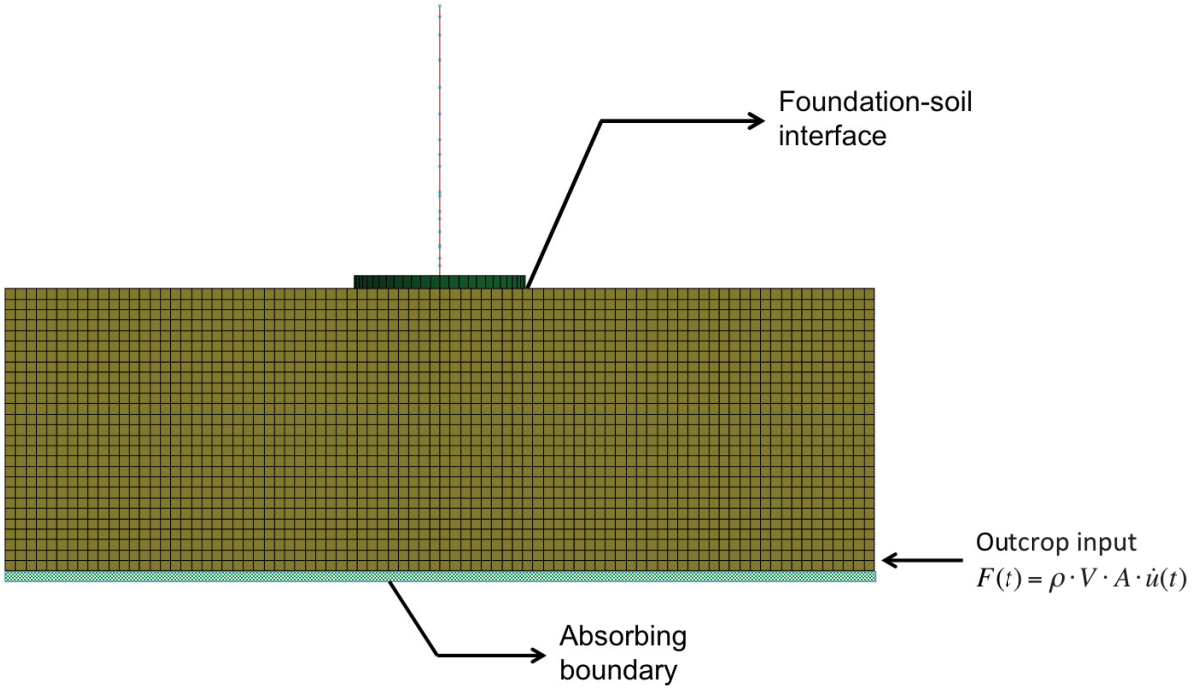

Figure 4-7: Procedure for ground motion input in the LS-DYNA model

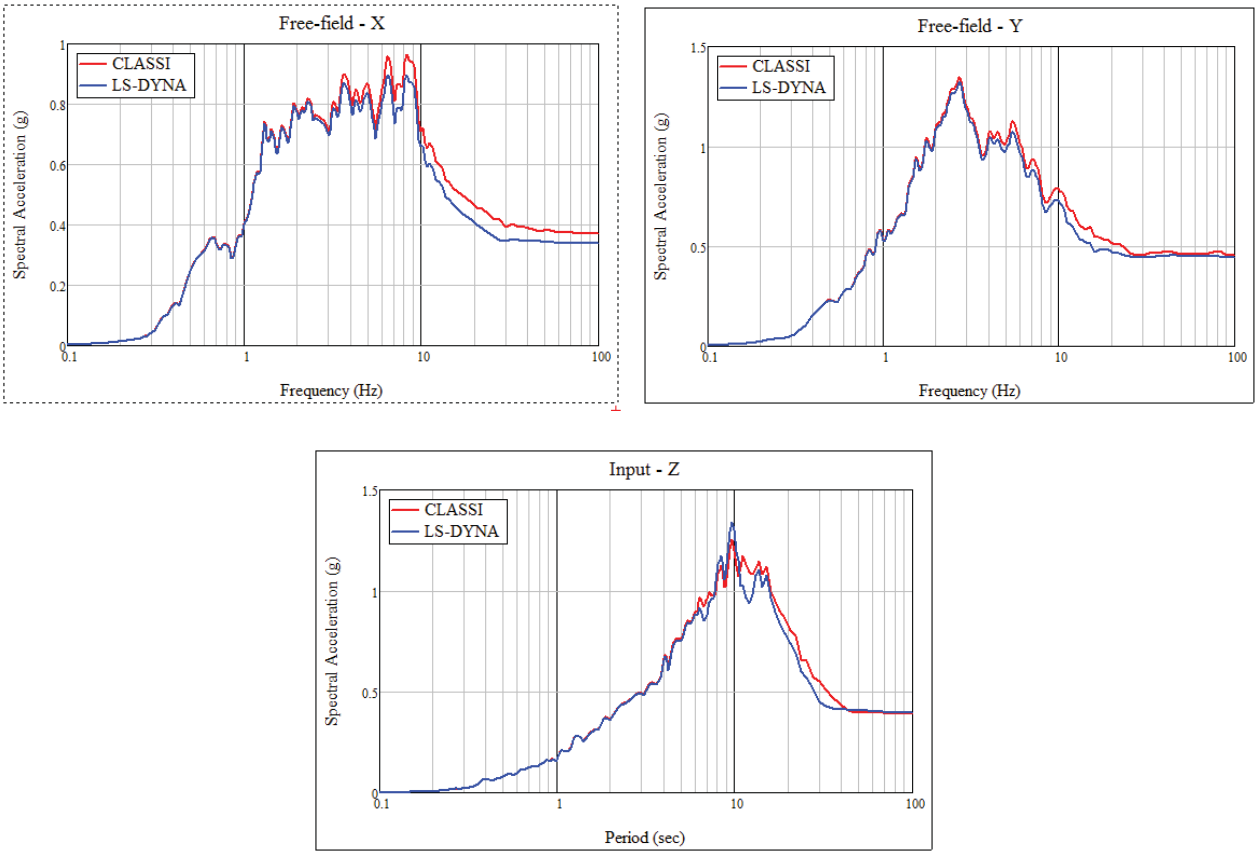

Figure 4-8: 5% damped response spectra of the free-field input acceleration in CLASSI and the free-field acceleration calculated using LS-DYNA

4.2.4 Foundation-soil interface modeling

Several approaches of modeling the foundation-soil interface can be adopted and the approach is chosen on a case-by-case basis. Since the representative NPP structure of this study is founded on the surface, it highly susceptible to foundation uplift in comparison with real nuclear structures that are usually partially embedded. The choice of surface foundation is intentional and is expected to demonstrate an extreme case of gapping and sliding.

Preliminary NLSSI analyses were performed by modeling the foundation-soil interface in LS-DYNA using the *CONTACT_AUTOMATIC_SURFACE_TO_SURFACE model. This contact model enables separation between the surfaces and simulates sliding behavior with Coulomb friction. A friction coefficient of 0.5 and a contact damping of 20% was used. The analysis was performed for one ground motion (simultaneous input in all three directions) at two intensity levels: reference PGAs of 0.4g and 0.8g. Figure 4-9 presents the basemat spectral accelerations calculated from these preliminary NLSSI analyses. The figure shows reasonable results for a reference PGA of 0.4g: the spectral accelerations calculated using linear and nonlinear analyses are almost equal, with a small reduction in peak spectral acceleration the Y direction from sliding. Predictably, a significant reduction in the spectral accelerations (at frequencies less than 10Hz) can be seen in responses to a reference PGA of 0.8g. However the spectral accelerations for frequencies above 10Hz are significantly amplified, which may be a combined result of the basemat impact on the soil due to uplift, as well as numerical noise. Given

that the amount of amplification is significant until 100Hz the results at these frequencies are likely spurious. Therefore, after several attempts in reducing the spurious response by changing the various parameters of the contact model, this approach to modeling the foundation-soil contact was ruled out for this study.

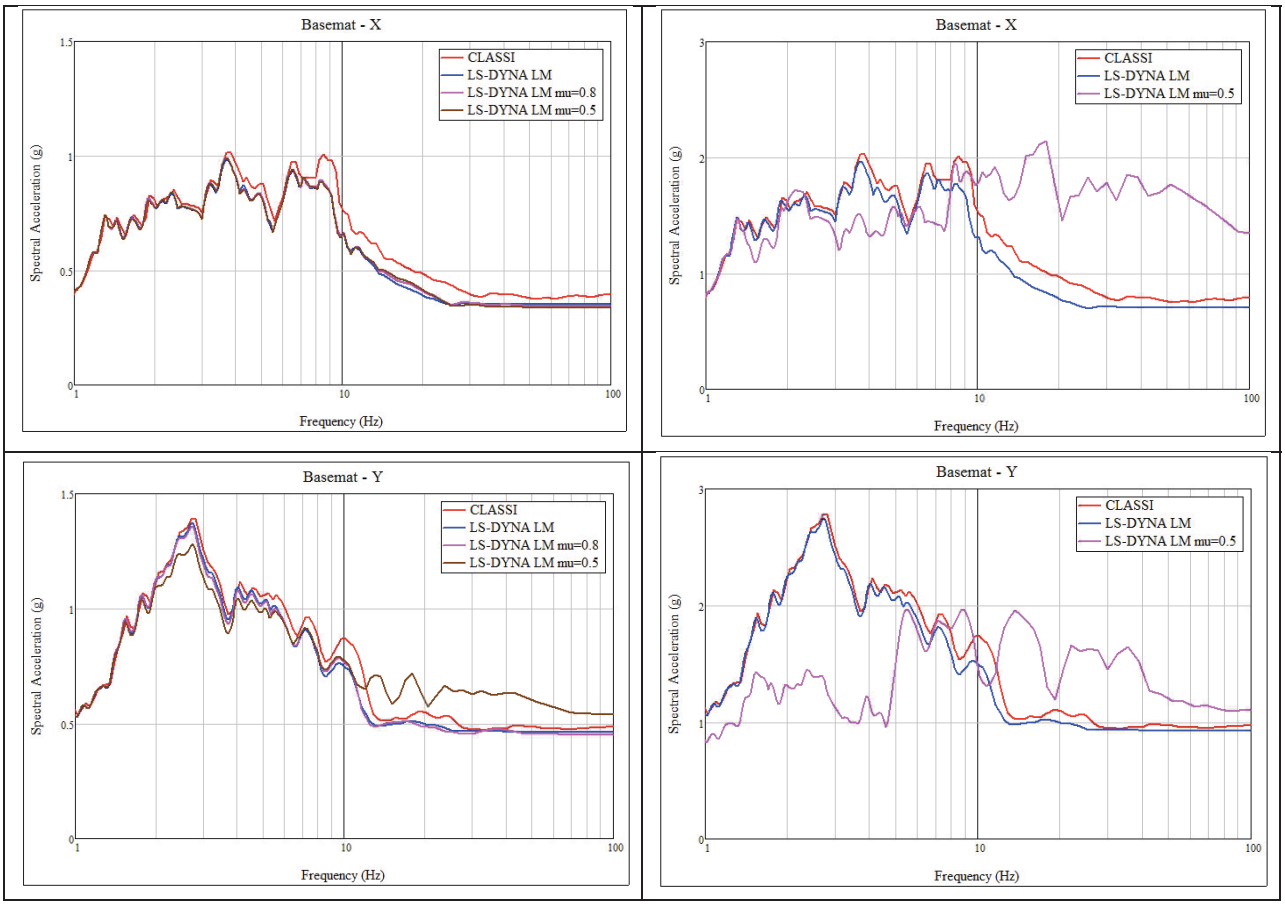

Figure 4-9: Spectral accelerations calculated using 1) CLASSI, 2) linear analysis in LS-DYNA and 3) nonlinear analyses in LS-DYNA of preliminary NLSSI analysis performed using LS-DYNA contact models for a 0.4g reference PGA (left) and 0.8g reference PGA (right)

Other approaches to simulate gapping and sliding were attempted including modeling the foundation-soil interface with very short seismic isolator elements. These elements were modeled as friction pendulum isolators using the *MAT_SEISMIC_ISOLATOR material model. A very large value was provided for the isolator surface radius, thereby making the structure sliding on an almost flat surface. Although this method provided slightly more reasonable results, penetrations were noticed at the foundation-soil interface, presumably due to insufficient vertical stiffness of the isolators. An attempt to increase the vertical stiffness resulted in an unstable analysis time step leading to discard of this approach.

The final approach involved modeling a thin layer of soil between the basemat and the soil. This layer, with the same plan dimensions as the basemat, is modeled using the *MAT_HYSTERETIC_SOIL model. This layer is illustrated in Figure 4-10. The material properties of this soil layer are chosen such that the shear strength of the layer is equal to the maximum

friction force for a given coefficient of friction and the weight of the structure. The shear strength (shear stress at failure) of the soil material is given by the equation

$$\tau_{max} = \frac{\mu W}{A} \qquad 4\text{-}1$$

where A is the maximum shear stress, μ is the coefficient of friction, W is the weight of the superstructure and basemat and A is the plan area of the basemat. These properties for the interface soil layer simulate a sliding behavior that is reasonably close to Coulomb friction. Simulation of gapping requires this soil layer to have almost zero strength in tension, which can be modeled directly by providing a very small value for the parameter P0 in input for *MAT_ HYSTERETIC_SOIL.

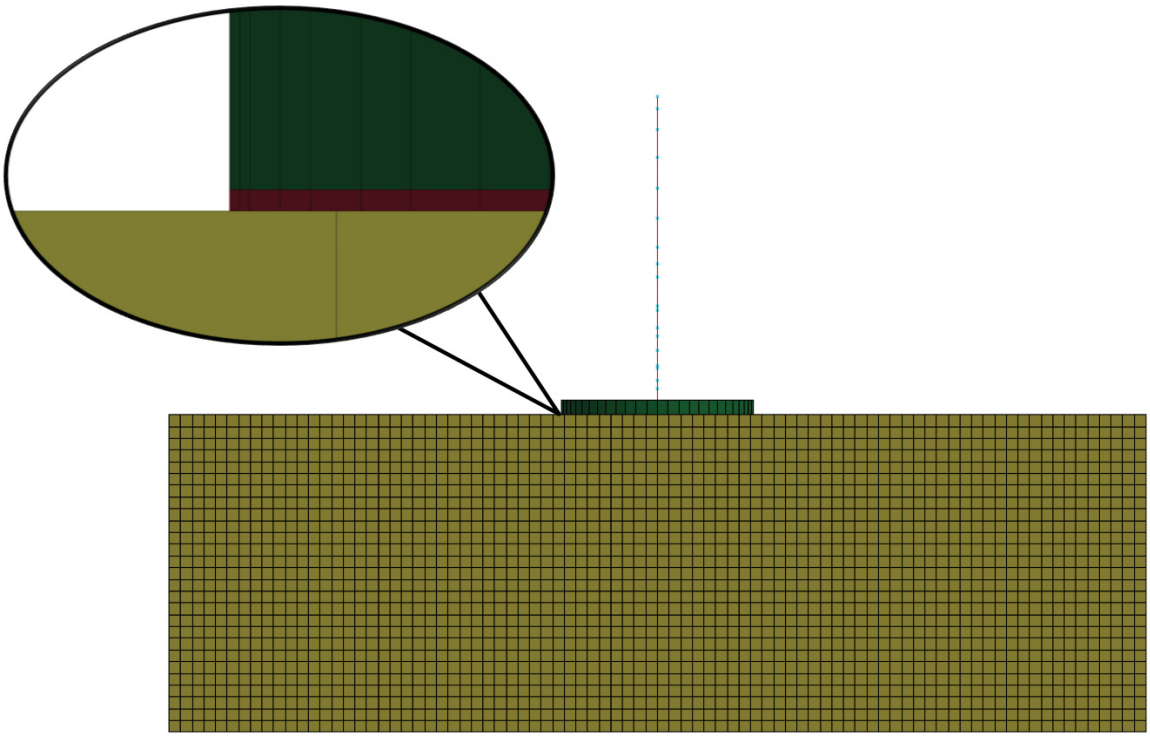

Figure 4-10: Thin soil layer in at the foundation-soil interface used in the final approach to simulating gapping and sliding in the present study

The input stress-strain curve provided for the interface layer for a friction coefficient of 0.7, 0.55 and 0.90, which correspond to the median, 16th percentile and 84th percentile values of the friction coefficients assumed for this study are presented in Figure 4-11 below. The figure also presents the corresponding stress-strain curves required for the layer to exactly simulate Coulomb friction. As shown in the figure, a small post-yielding stiffness is provided for the interface layer to avoid numerical instabilities. Additionally, the shear strength of the soil layer is approximately equal to the required shear strength required to simulate Coulomb friction.

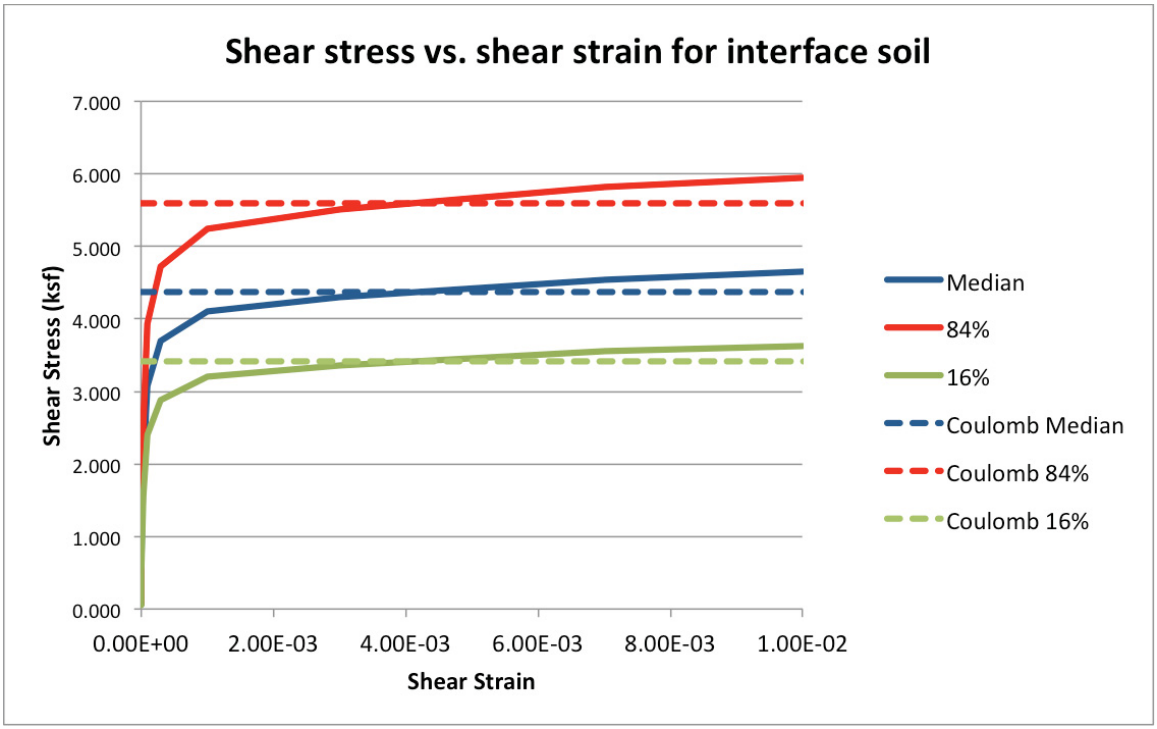

Figure 4-11: Input stress-strain backbone curves used for the foundation-soil interface layer to approximate Coulomb friction

4.2.5 Assembling the NLSSI model

After verifying that the structural models in CLASSI and LS-DYNA are equivalent, SSI analyses are performed for the representative NPP structure in LS-DYNA. The NPP structure is supported by a surface basemat that is 10ft thick and 131ft in diameter. This basemat is assumed to be rigid and is modeled with the *MAT_RIGID material model in LS-DYNA. The soil domain is assumed to be a uniform halfspace with the soil properties listed in Table 2-1. The soil is assumed to be elastic and is modeled using the *MAT_ELASTIC material model. Prior to performing a nonlinear SSI analysis that simulates gapping and sliding at the foundation, a linear model is analyzed and the results are compared with CLASSI for verification. In this linear model, the basemat is 'tied' to the soil surface, and no gapping or sliding is permitted. After the linear model is verified to produce the same response as CLASSI, it is modified to include contact models at the foundation-soil interface and the nonlinear analyses are performed. The procedure for SSI analysis in LS-DYNA is briefly described in the sections that follow. Results from linear analysis are presented in Section 4.3 and the results from nonlinear analyses are presented in Section 4.4.

4.3 Linear SSI analysis and benchmarking against CLASSI

A linear analysis, in which there is no separation at the foundation-soil interface, is performed in LS-DYNA to verify the SSI model by comparing the results to those calculated using CLASSI. Since CLASSI performs a linear analysis, there should be a very close match between the linear responses calculated using LS-DYNA and CLASSI. Following the procedure described in Section 4.2, a linear analysis is performed in LS-DYNA for one set (three

directions) of ground motions. In this section results of this linear analysis are presented and compared with those from CLASSI.

In the linear analysis, the foundation is attached to the elastic soil using the *CONSTRAINED_EXTRA_NODES option, which constrains the basemat and soil nodes at the basemat-soil interface to move together. The thin soil layer at the foundation-soil interface is notmodeled in the linear analysis. Figure 4-12 and Figure 4-13 present the CLASSI and LS-DYNA results for the linear analysis at the center of the basemat and the internal structure, respectively. The figures show that the linear analyses in CLASSI and LS-DYNA produce almost similar results. LS-DYNA results in slightly smaller spectral accelerations mainly because of the smaller free-field accelerations. Additionally, it should be noted that the SSI analysis procedure in CLASSI does not account for kinematic interaction, unlike LS-DYNA. The kinematic interaction in LS-DYNA can also contribute to the slight reduction in spectral accelerations, especially in the higher frequencies.

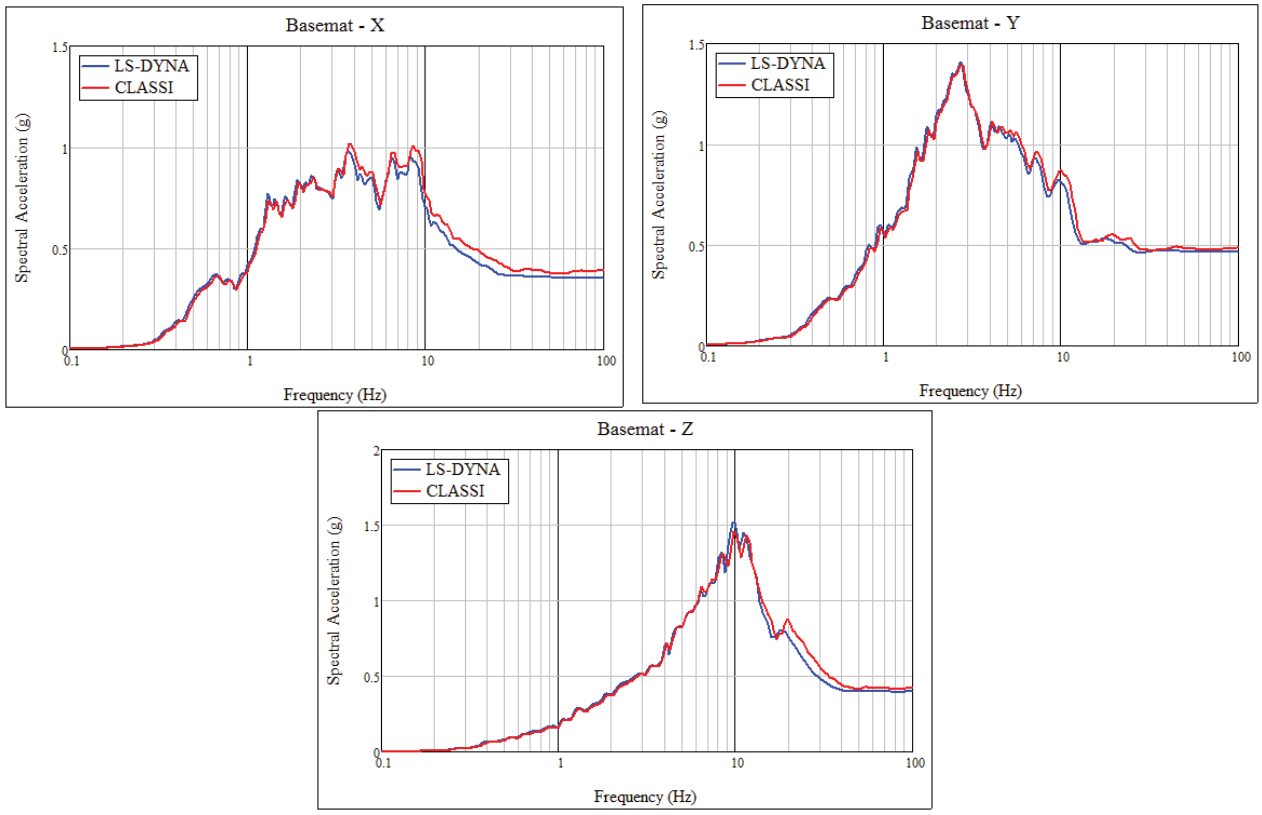

Figure 4-12: 5% damped acceleration response spectra on the basemat calculated using linear SSI analyses in CLASSI and LS-DYNA

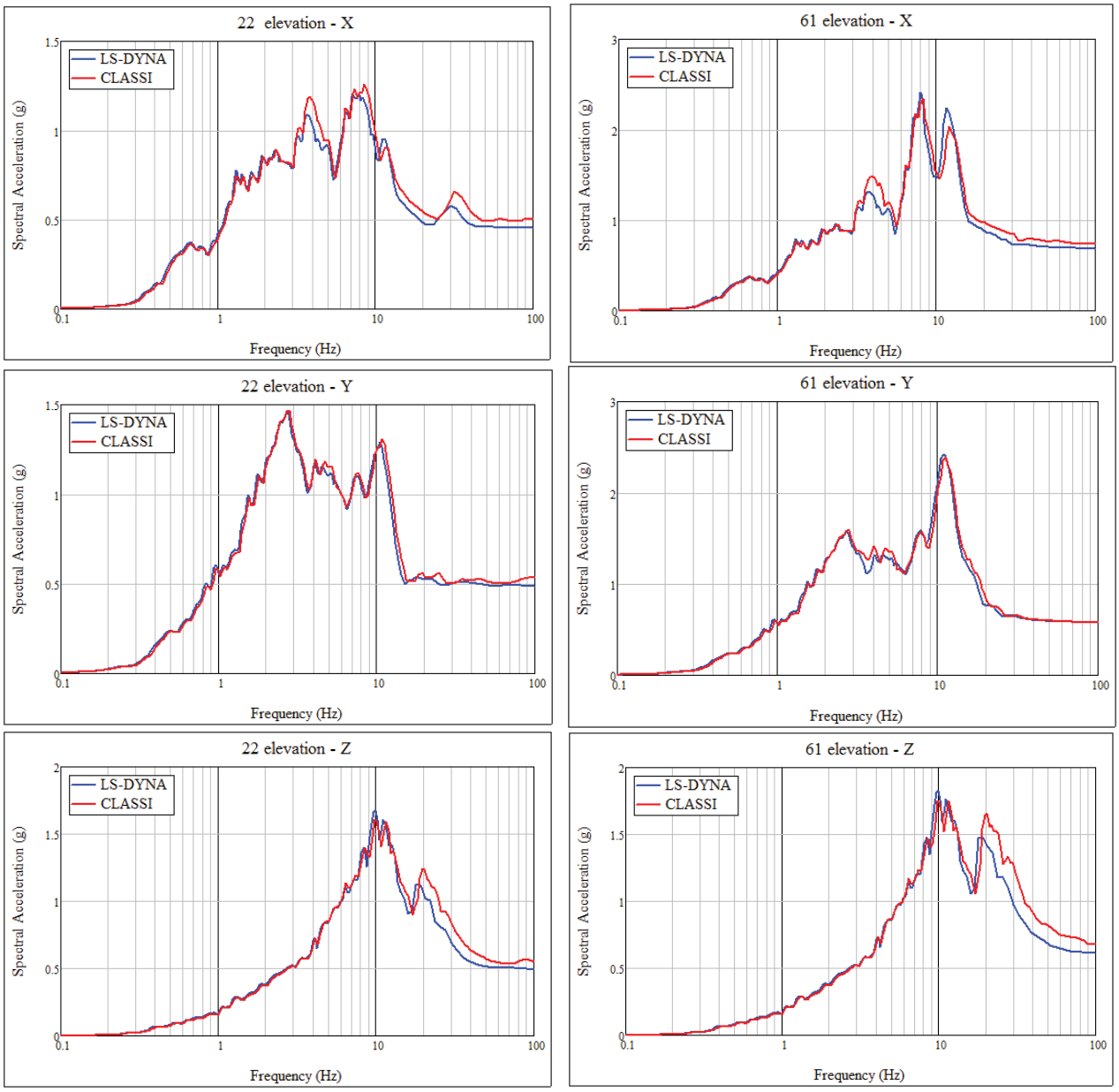

Figure 4-13: 5% damped acceleration response spectra in the internal structure at 22ft elevation (left) and 61ft elevation (right) calculated using linear SSI analyses in CLASSI and LS-DYNA

4.4 Nonlinear SSI analysis

Nonlinear analysis is performed after modifying the linear model (benchmarked in the previous section) by including the foundation-soil interface layer described in Section 4.2.4. For the study presented in this report, the nonlinear analyses are performed for three ground motions at four intensities as described in Section 4.5. Results for one of the ground motion (and using median soil and structure properties) are presented in this section. Figure 4-14 presents the spectral accelerations calculated at the basemat and Figure 4-15 presents the ISRS calculated at 22’ and 61’ elevations.

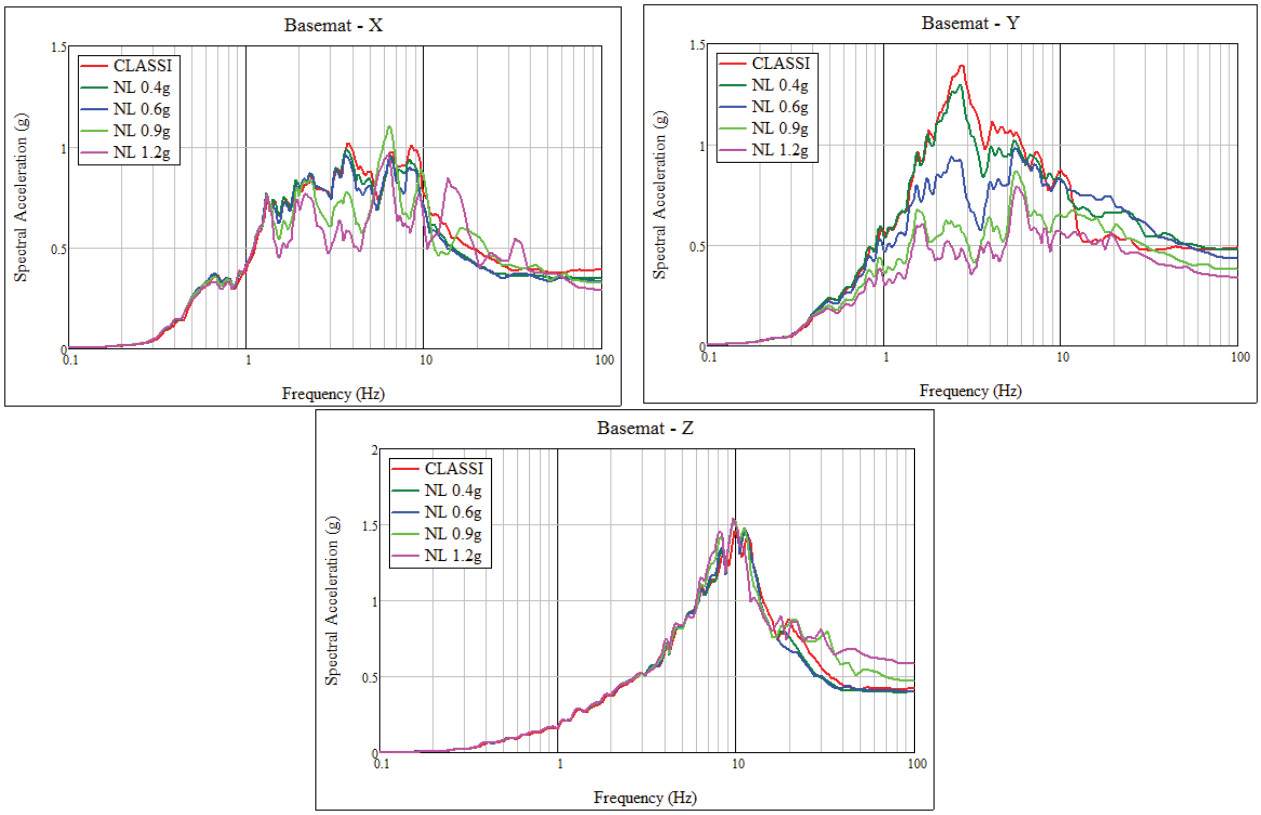

Figure 4-14: 5% damped spectral accelerations at the center of the basemat calculating using CLASSI and at four ground motion intensities in LS-DYNA (reference PGAs of 0.4g, 0.6g, 0.9g and 1.2g). The LS-DYNA results at higher intensities are scaled down to 0.4g in this figure.

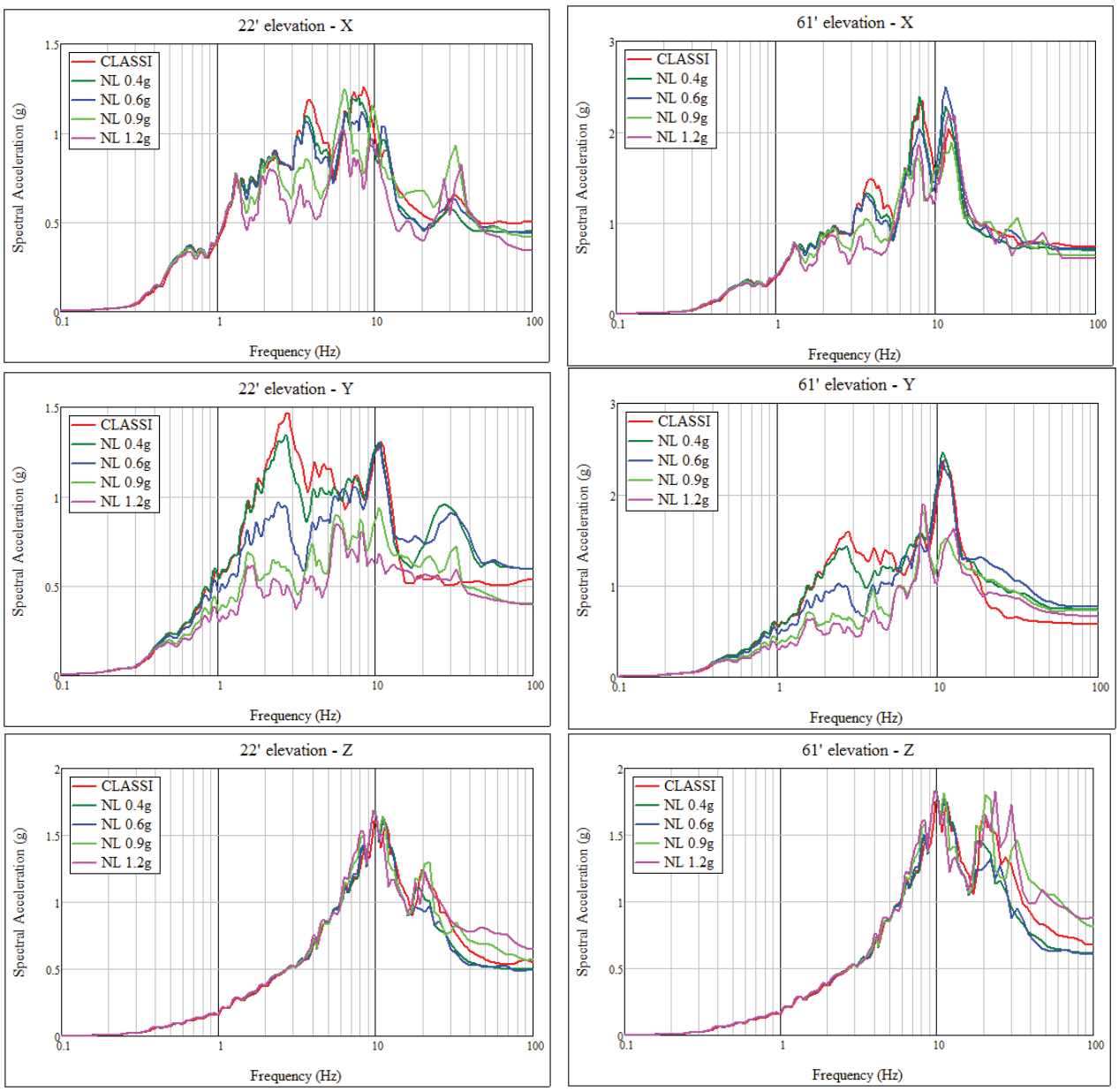

Figure 4-15: 5% damped spectral accelerations in the internal structure at 22' elevation (left) and 61' elevation (right) calculating using CLASSI and at four ground motion intensities in LS-DYNA (reference PGAs of 0.4g, 0.6g, 0.9g and 1.2g). The LS-DYNA results at higher intensities are scaled down to 0.4g in this figure.

The following observations and conclusions can be made from the results presented in Figure 4-14 and Figure 4-15:

1. The nonlinear results at a reference PGA of 0.4g are very close to the CLASSI results, except for a small decrease in the peak spectral acceleration in the Y direction. This shows that sliding has just initiated at a reference PGA of 0.4g.
2. The nonlinear results in X and Y directions gradually deviate from the linear results with increasing reference PGA. The normalized spectral accelerations calculated using nonlinear analyses are generally decreasing with increasing reference PGA at frequencies

smaller than 10Hz. This decrease is due to the energy dissipated in sliding and results in reduced in-structure demands. The results show that this reduction can be significant for frequencies smaller than 10Hz.

3. At the higher frequencies, nonlinear effects result in an increase in the response. This is likely due to gapping, and the resulting impact of the basemat on the soil surface. This result shows that the geometric nonlinearities can result in an increase in the in-structure response at higher frequencies.
4. The results in the Z direction are almost unchanged until about 20Hz, indicating that the geometric nonlinearities do not generally affect the vertical response. At the higher frequencies, the Z direction response increases, likely due to the impact from gapping.

4.5 Seismic component capacity distributions

The component capacity distribution describes the conditional probability of failure given the in-structure spectral acceleration. The spectral acceleration capacity distributions listed in Table 4-2 were derived from the component seismic fragilities (Section 3.2). The median spectral acceleration capacity represents the 5% damped in-structure spectral acceleration in the controlling direction of motion at the median component frequency for which the net median demand on the controlling element equals its median capacity. The variability is represented by the lognormal standard deviation for component capacity.

Table 4-2: Component spectral acceleration capacity distributions

Component	Floor	Direction	Frequency (Hz)	SA_m	β_c
Pump 670-M-11	EL 61’	X	20	7.46g	0.16
Battery 670-E-59	EL 22’	Y	8.3	3.10g	0.10
Distribution Panel 670-E-23	EL 61’	X	7.5	6.24g	0.42
Block Wall 2B-G2-1	EL 22’	Y	0.89	0.73g	0.17
Switchgear 670-E-1	EL 61’	Y	5 - 10	4.8g	0.42

4.6 Component response probability distributions

We performed a deterministic seismic response analysis using three structure/soil models and a limited number of time-history sets in order to develop a preliminary estimate of the nonlinear response distribution. The deterministic response analysis followed the following procedure:

1. Ground motion input consisted of three sets of acceleration time histories. These sets were selected from the original 30time-history sets used in Section 3.1. They therefore included variability in the X and Y direction spectra about the geometric mean UHS.
2. We used three structure/soil models to represent best-estimate (BE), lower-bound LB) stiffness, and upper-bound (BE) stiffness. The BE case combined the 84% NEP structure stiffnesses, soil stiffnesses, and soil coefficient of friction. The LB case used the 16% NEP values of these parameters.

3. We computed the average ISRS for each of the BE, LB, and UB cases.
4. We defined the median response as the average of the three average ISRS plots.
5. We defined the 84% NEP response for structure and soil property uncertainty as the envelope of the three average ISRS.
6. We defined the 84%NEP response for time-history uncertainty as the envelope of the BE ISRS, compared to the average BE ISRS.

The resulting ISRS are shown in Figures 4-16 through 4-19. Comparison of the plots in these figures demonstrates that the ISRS do not scale linearly with the PGA. The nonlinear effects are frequency-dependent and therefore the spectral shapes of the ISRS are not preserved. The pots also show the X-direction median spectral accelerations in the frequency range of 1 Hz to 4 Hz are generally higher than the Y-direction results. This discrepancy is due to the particular characteristics of the 3 time-histories that were used in this deterministic response analysis, which happened to have a directional bias towards the X-direction in this frequency range. Use of the full 30-set suite of time-histories in the full probabilistic analysis will alleviate this bias in the horizontal directional variability.

We estimated the median demands for each equipment component as the median spectral acceleration at the controlling direction and frequency (Table 4-2). Probabilistic ISRS do not typically have significant valleys between peaks as do the deterministic ISRS. The only component whose demand is controlled by a frequency where there is a nearby valley is Battery 670-E-59. Battery 670-E-59 is controlled by Elev. 22ft Y-direction spectral acceleration at 8.3 Hz. Therefore, the median demand for this battery was defined as the average spectral acceleration calculated within a range of 6.8 Hz and 10.1 Hz, which represented ±one standard deviation on the equipment frequency.

The response variabilities were estimated as follows

1. Structure response variability was calculated using the SRSS method from two components: time-history variability and structure/soil property uncertainty.
    - Lognormal standard deviation due to time-history variability was calculated based on the ratio of the envelope BE spectral acceleration to the average BE spectral acceleration, with a minimum value of 0.10.
    - Lognormal standard deviation due to structure/soil property uncertainty was calculated based on the ratio of the 84% spectral acceleration to the median spectral acceleration. A minimum value of 0.10 was imposed with the exception of the block wall, which has a low frequency (less than 1 Hz).
2. The other variabilities were computed using procedures and assumptions similar to the linear analysis case for each component (Section 3.2.1).

The preliminary median spectral accelerations are listed in Table 4-3. The lognormal standard deviations are listed in Table 4-4. The corresponding results from the linear CLASSI analysis at 0.4g PGA are shown for comparison. The results show an acceptable match between the linear and nonlinear response distributions at the 0.4g PGA where little nonlinearity is observed to occur in the analysis.

Table 4-3: Component median spectral acceleration preliminary demands based on deterministic response analysis, $SA_{m,R}$, (g)

Component	0.4 g PGA (Linear)	0.4g PGA	0.6g PGA	0.9g PGA	1.2g PGA
Pump 670-M-11	0.88	0.87	1.42	2.19	3.01
Battery 670-E-59	1.09	1.08	1.56	2.02	2.29
Distribution Panel 670-E-23	1.56	1.56	2.23	3.45	4.34
Block Wall 2B-G2-1	0.49	0.49	0.7	0.97	1.16
Switchgear 670-E-1	1.01	0.95	1.42	1.95	2.16

Table 4-4: Component response preliminary lognormal standard deviations based on deterministic response analysis

Component	0.4g PGA (Linear)	0.4g PGA	0.6g PGA	0.9g PGA	1.2g PGA
Pump 670-M-11	0.38	0.34	0.30	0.32	0.30
Battery 670-E-59	0.26	0.29	0.27	0.30	0.31
Distribution Panel 670-E-23	0.41	0.39	0.43	0.35	0.39
Block Wall 2B-G2-1	0.22	0.2	0.19	0.18	0.24
Switchgear 670-E-1	0.21	0.21	0.21	0.31	0.28

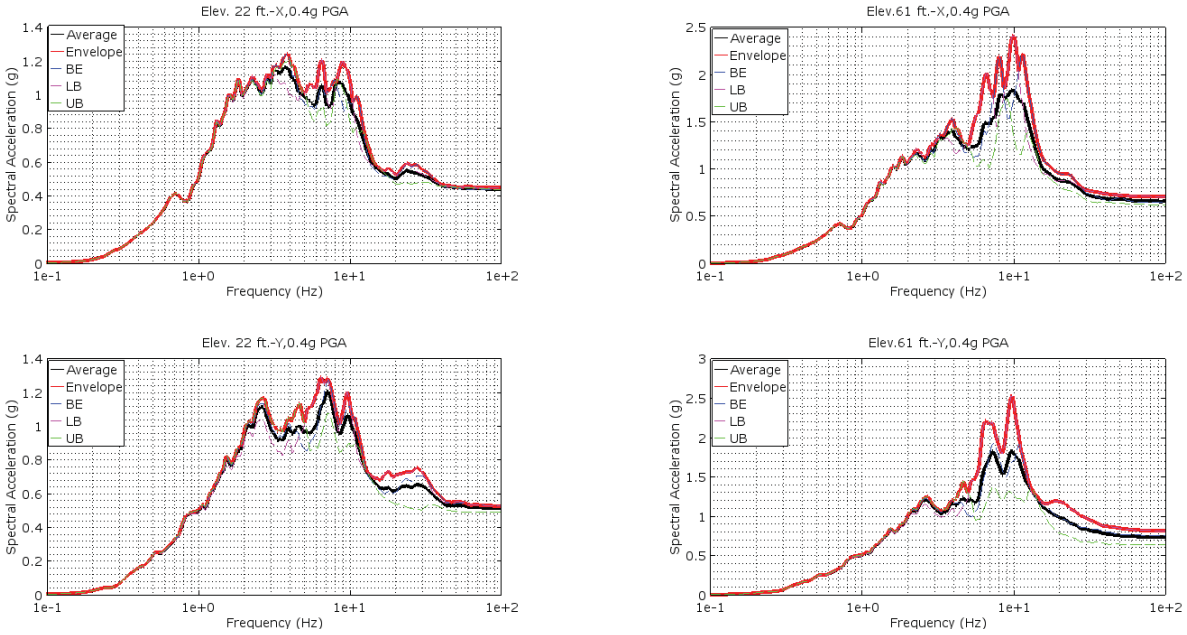

Figure 4-16: 5% damped spectral accelerations in the internal structure at 22' elevation (left) and 61' elevation (right) from the deterministic response analysis at 0.4g PGA

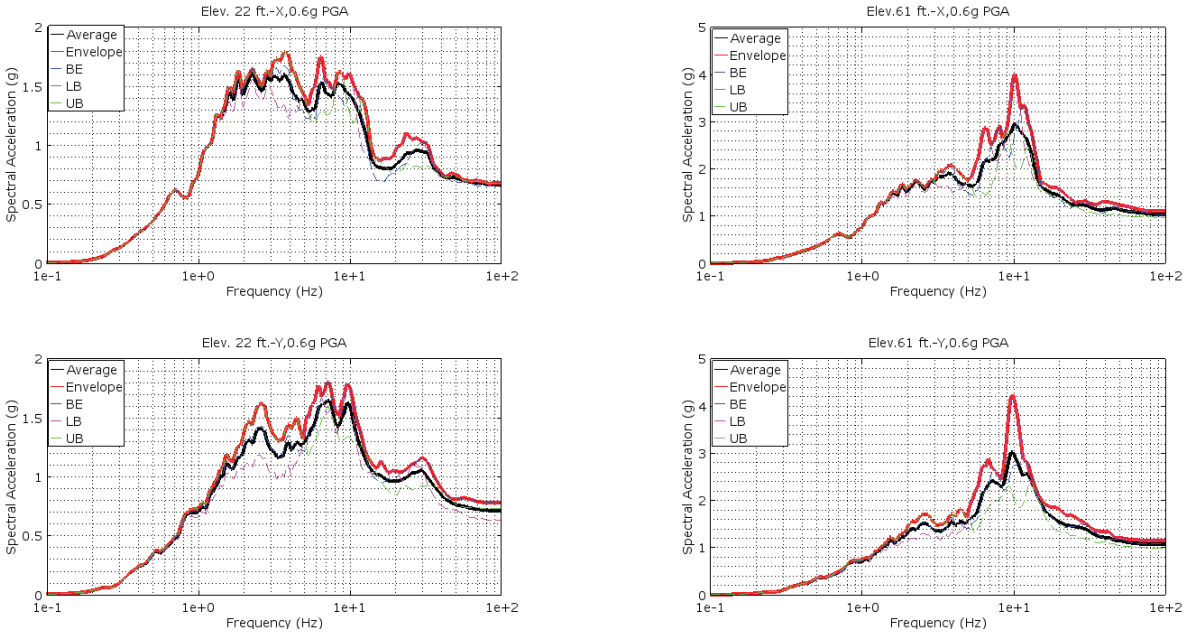

Figure 4-17: 5% damped spectral accelerations in the internal structure at 22' elevation (left) and 61' elevation (right) from the deterministic response analysis at 0.6g PGA

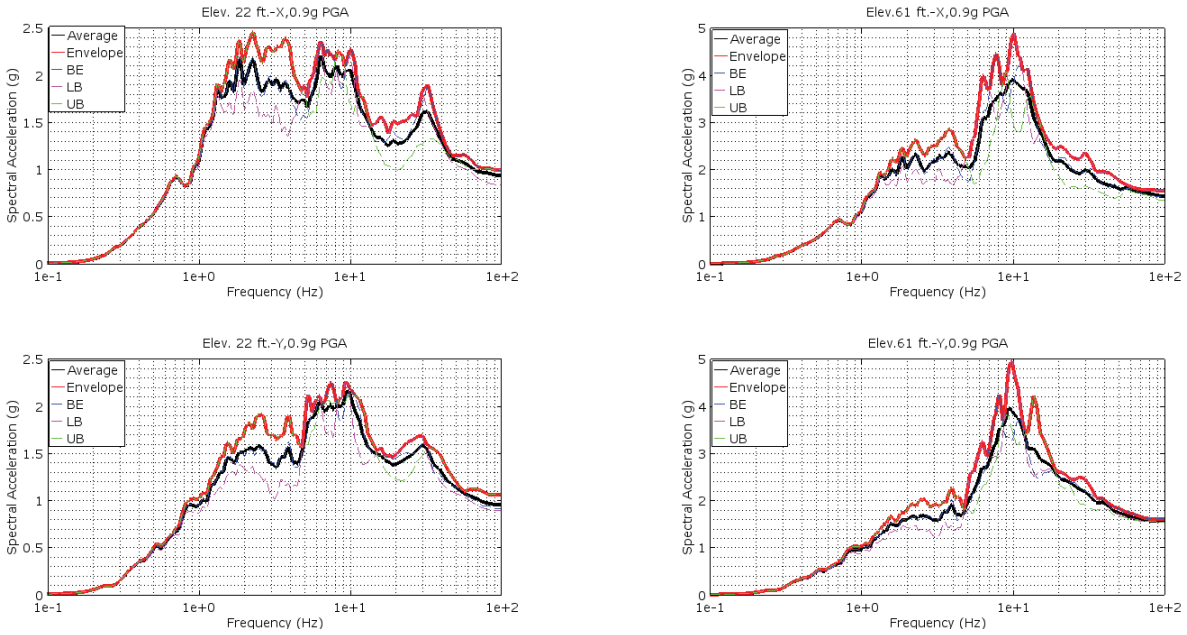

Figure 4-18: 5% damped spectral accelerations in the internal structure at 22' elevation (left) and 61' elevation (right) from the deterministic response analysis at 0.9g PGA

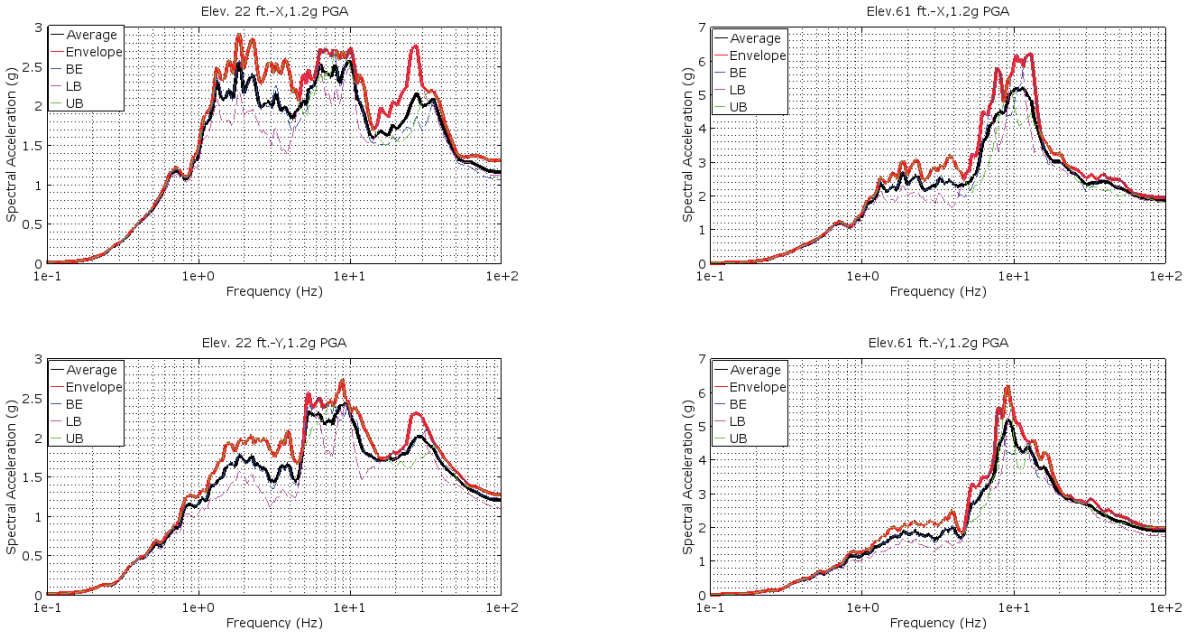

Figure 4-19: 5% damped spectral accelerations in the internal structure at 22' elevation (left) and 61' elevation (right) from the deterministic response analysis at 1.2g PGA

4.7 Seismic component conditional probabilities of failure

The conditional probabilities of component failure are calculated explicitly by convolution of the component capacity distributions and the probabilistic response distributions at each PGA level. They are summarized in Table 4-5. Figure 4-20 shows the conditional probabilities of component failures given the PGA for the traditional SPRA approach in solid lines, compared to the estimated values using the advanced SPRA approach. These preliminary results suggest that the latter probabilities are generally lower than the traditional SPRA probabilities at higher intensity ground motions. The preliminary results also suggest that some of these latter probabilities may not follow a lognormal distribution. More nonlinear probabilistic response analyses and more (higher) PGA levels are required in order to further examine these observations and generalize the conclusions drawn from them.

Table 4-5: Component conditional probabilities of failure

Component	0.4g PGA	0.6g PGA	0.9g PGA	1.2g PGA
Pump 670-M-11	0.0000	0.0000	0.0003	0.0038
Battery 670-E-59	0.0003	0.0085	0.0878	0.1762
Distribution Panel 670-E-23	0.0078	0.0435	0.1392	0.2632
Block Wall 2B-G2-1	0.0644	0.4346	0.8745	0.9423
Switchgear 670-E-1	0.0003	0.0047	0.0422	0.0568

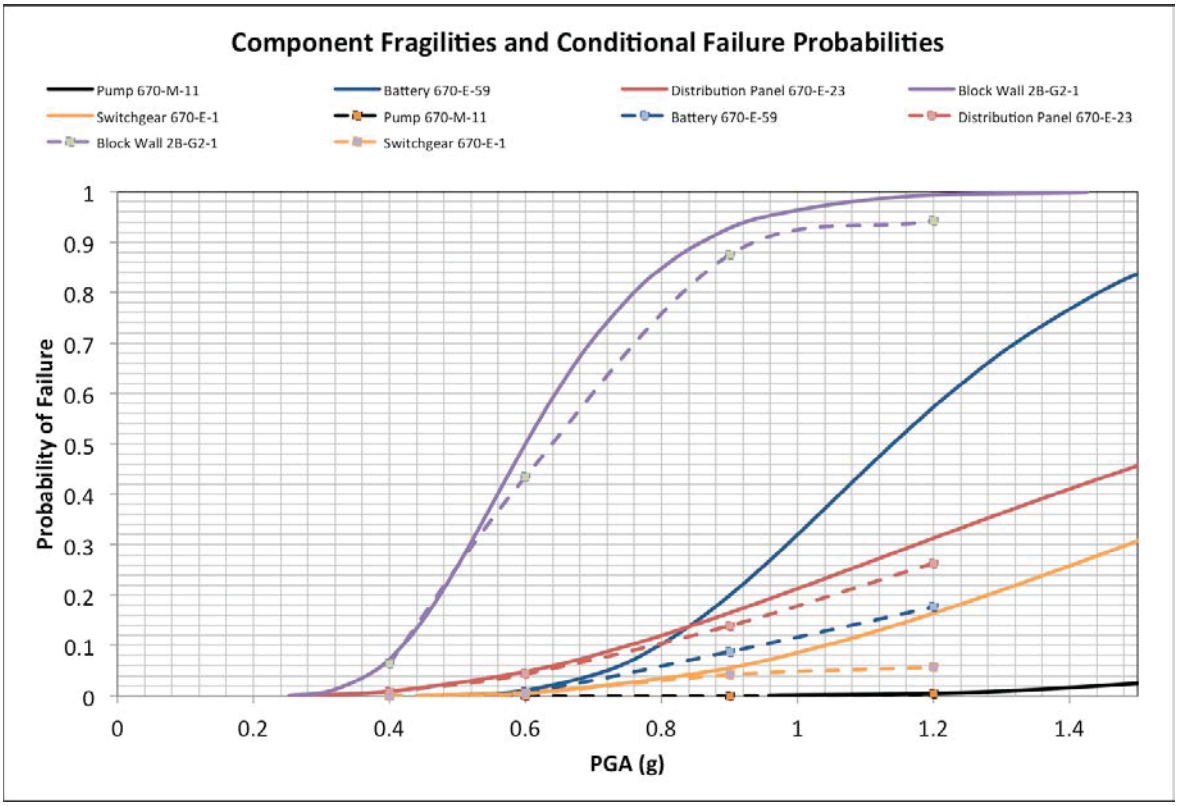

Figure 4-20: Component fragilities and conditional probabilities of failure calculated using the traditional and advanced PRA approaches

5. Summary and Conclusions

This report presents the calculation of seismic fragilities in a nuclear power plant structure using two approaches:

- The traditional SPRA approach, which involves linear seismic SSI response analysis and the assumption that the component demands increase linearly with increasing ground motion intensity
- An advanced SPRA approach that considers geometric nonlinear effects at the foundation and rejects the assumption of linear increase in demand with increasing ground motion intensity.

The study in this report considered an idealized nuclear power plant structure (borrowed from the SASSI2000 user manual), a soil profile representative of the ATR site at INL and a seismic hazard representative of the Western United States. The system under consideration for risk analysis is the Emergency Cooling Pump at ATR. Five components of this system are considered: Pump 670-M-11, Battery-670-E-59, Distribution Panel 670-E-23, Block Wall 2B-G2-1 and Switchgear 670-E-1.

Linear analyses are performed by SGH using the industry-standard nonlinear SSI analysis code, CLASSI. SGH also performed the fragility calculations for the above-listed components and used the linear analysis results to calculate the seismic component fragilities.

Nonlinear SSI analyses are performed by INL using the NLSSI methodology (developed by INL) for a limited number of ground motions at four reference intensities. The nonlinear SSI analysis results clearly showed that the in-structure demands do not increase linearly with increasing intensity. The in-structure responses are lower than the corresponding linear responses for most frequencies. For some cases the in-structure responses are higher than the linear counterparts at frequencies larger than 10Hz.

SGH estimated nonlinear response distribution parameters from these preliminary NLSSI results and used these distributions to calculate preliminary estimates of the component seismic fragilities. A comparison of the response distributions showed that the median demands calculated considering the nonlinear effects do not scale linearly unlike in traditional SPRA. A comparison between the component fragilities showed that the conditional probabilities of failure for given PGA values estimated using advanced SPRA are generally smaller than those calculated using the traditional approach. The advanced SPRA calculations are currently being updated with results from a larger set of NLSSI analyses and the resulting component fragilities, and system fragilities will be presented in a future report.

6. References

Bathe, K.-J. (1996). "Finite Element Procedures." Prentice Hall, Upper Saddle River, New Jersey.

Bolisetti, C., and Whittaker, A. S. (2015). "Site Response, Soil-Structure Interaction and Structure-Soil-Structure Interaction for Performance Assessment of Buildings and Nuclear Structures." Multidisciplinary Center for Earthquake Engineering Research (MCEER), University at Buffalo, The State University of New York, Buffalo, NY.

Bolisetti, C., Whittaker, A. S., and Coleman, J. L. (2015). "Frequency- and Time-Domain Methods in Soil-Structure Interaction Analysis." *Nuclear Engineering and Design*, Under Review.

Coleman, J. L., Bolisetti, C., and Whittaker, A. S. (2015). "Time-Domain Soil-Structure Interaction Analysis for Nuclear Facilities." *Nuclear Engineering and Design*, Accepted, in press. .

Computers and Structures Inc. (2011). Computer Program: SAP2000 - Structural Analysis Program, Version 11.0.0. Computers and Structures, Inc., Berkeley, California.

Livermore Software Technology Corporation (LSTC). (2009). "LS-DYNA Theory Manual." Livermore, California.

Livermore Software Technology Corporation (LSTC). (2013). "LS-DYNA Keyword User's Manual - Version R 7.0." Livermore, California.

Lysmer, J., Ostadan, F., and Chin, C. (1999). Computer Program: SASSI2000 - A System for Analysis of Soil-Structure Interaction. University of California, Berkeley, California.

Ostadan, F. (2006). "SASSI2000: A System for Analysis of Soil Structure Interaction - User's Manual." University of California, Berkeley, California.

Spears, R., and Coleman, J. (2014). "Nonlinear Time Domain Soil-Structure Interaction Methodology Development." INL/EXT-14-33126, Idaho National Laboratory, Idaho Falls, Idaho.

Willford, M., Sturt, R., Huang, Y., Almufti, I., and Duan, X. (2010). "Recent Advances in Nonlinear Soil-Structure Interaction Analysis using LS-DYNA." *Proceedings of the NEA-SSI Workshop*, October 6-8, Ottawa, Canada.

Luco, J.E. and H.L. Wong, Soil-Structure Interaction: A Linear Continuum Mechanics Approach (CLASSI), Report No. CE79-03, University of Southern California, Los Angeles, CA, 1980.

Jack R. Benjamin and Associates, Inc. and RPK Structural Mechanics Consulting, Methodology for Developing Seismic Fragilities, prepared for the Electric Power Research Institute, EPRI TR-103959, Palo Alto, CA, 1994.

Kennedy, R., G. Hardy, and K. Merz, Seismic Fragility Application Guide Update, prepared for the Electric Power Research Institute, EPRI 1019200, Palo Alto, CA, 2009.

U.S. Department of Energy, Seismic Evaluation Procedure for Equipment in U.S. Department of Energy Facilities, DOE/EH-0545, Washington, D.C., March 1997.

ARES Corporation, Anchorage Evaluation of Group F-12, Calculation No. 0602301.01-S-113, Revision 0, Santa Ana, CA, 2008.

Simpson Gumpertz & Heger, Inc., Seismic Fragility Evaluation of Batteries 670-E-58 and 670-E-59, Calculation No. 098122-CA-18, Revision 0, Newport Beach, CA, 2010.

Idaho National Laboratory, Seismic Evaluation for Electrical Cabinets 670-E-23, 670-E-28, 670-E-103, 670-E-105, 670-E-116, and 670-E-459, EDF-4316, Idaho Falls, ID, 2003.

ARES Corporation, Anchorage Evaluation of Group F-19, Calculation No. 0602301.01-S-109, Revision 0, Santa Ana, CA, 2008.

Electric Power Research Institute, Seismic Verification of Nuclear Plant Equipment Anchorage (Revision 1), Volume 1: Development of Anchorage Guidelines, EPRI NP-5228-SL, Revision 1, Vol. 1, Palo Alto, CA, 1991.

Electric Power Research Institute, A Methodology for Assessment of Nuclear Power Plant Seismic Margin, EPRI NP-6041-SL, Revision 1, Palo Alto, CA, 1991.

ARES Corporation, Seismic Evaluation of the Concrete Block and Shielding Walls in TRA-670, Calculation No. 0602301.01-S-007, Revision 0, Santa Ana, CA, 2008.

APPENDIX A

Numerical Tool Development

The team at University at Buffalo has developed the numerical capability to model dynamic saturated porous media in MOOSE. Their report is presented below.

Development of u-P-U capability in MOOSE — progress report

M. V. Sivaselvan, Nicholas Oliveto and Andrew Whittaker
{mvs,noliveto,awhittak}@buffalo.edu
Department of Civil, Structural and Environmental Engineering and MCEER
University at Buffalo, 212 Ketter Hall, Buffalo, NY 14260

September 25, 2015

1 Background

The goal of this project is to implement a *three-field* formulation of the dynamics of saturated porous media in the Multiphysics Object Oriented Simulation Framework (MOOSE). Dynamics of porous media are of interest in a variety of fields including mechanics of saturated and partially saturated soil, porous biological materials and petroleum reservoirs. In particular, our motivation here is to simulate and understand the dynamic response of saturated soil under earthquakes and the subsequent soil liquefaction process [1–3].

Partial differential equation (PDE) models of the dynamics of saturated porous media are based on representing the porous medium as a solid skeleton filled with fluid. Such models contain three fields — the skeleton displacement (u), the velocity of the fluid relative to the skeleton, or Darcy velocity (w), and the pressure of the fluid contained in the skeleton, or the pore pressure (p). Various finite element formulations are possible for these PDE models — three-field (u-w-p) formulations and two-field (u-p or u-w) formulations [1]. A majority of current implementations are based on two-field formulations obtained by eliminating either the Darcy velocity w, resulting in a u-p formulation [3–10], or eliminating the pressure, leading to a u-w formulation [1, 11–15]. However, here we pursue a three-field formulation motivated by the following considerations.

1. The Darcy velocity, w, cannot be eliminated from the formulation unless the relative acceleration of the fluid is zero (see equation $(1)_2$ below). Thus a u-p formulation is reasonable only for scenarios in which the acceleration of the fluid relative to the solid skeleton is small. Similarly, the pore pressure, p, cannot be eliminated, and thus a u-w formulation is not possible, unless the combined flexibility of the skeleton material and the fluid is non-zero (see equation $(1)_3$ below). Therefore, to realistically model phenomena such as saturated soil-foundation-structure interaction in earthquakes, liquefaction and cyclic mobility, where the relative acceleration of the fluid could be substantial, and the skeleton material and fluid are relatively incompressible, a three-field formulation is necessary. This has also been pointed out by Jeremić et al. [2, 16, 17].

2. Since the u-p formulation amounts to solving for pressure and skeleton displacement as primary variable fields, post-processing in needed to compute the velocity field from the pressure gradient. The Darcy velocity obtained from a u-p formulation is consequently of lower accuracy [18, 19].

3. Both pressure and flux boundary conditions can be applied directly with a three-field formulation, but require special treatment with a two-field formulation [20].

4. Presence of the fluid velocity field in an explicit fashion in the formulation will also allow for poromechanics to be more readily coupled with transport phenomena in MOOSE.

In this report, we describe our approach to implementing a three-field formulation of the dynamics of porous media in MOOSE, indicate the current status of this effort, and outline the tasks that remain to be completed.

2 Governing equations

We begin with the set of equations developed by Biot [21] to describe dynamics of porous media. We impose the following restrictions, which are appropriate for the response of saturated soils: (i) the skeleton material (i.e., soil particles)and the fluid are incompressible; (ii) there is a single fluid phase (i.e., the soil is fully saturated); (iii) the skeleton has isotropic linear elastic behavior (nonlinear material models can be easily substituted later in MOOSE); (iv) fluid flow follow a linear isotropic form of Darcy's law; (v) kinematics are linearized (also resulting in constant porosity); (vi) the additional apparent mass used in Biot's equations is negligible. Then the governing equations are [22]

$$\begin{aligned} \rho\ddot{u} \quad &+ \rho^{\mathrm{f}}\dot{w} \quad - \nabla\cdot(\sigma - pI) = 0 \\ \rho^{\mathrm{f}}\ddot{u} \quad &+ \frac{\rho^{\mathrm{f}}}{\phi}\dot{w} \quad + \frac{\rho^{\mathrm{f}}g}{K}w + \nabla p \;= 0 \\ \nabla\cdot\dot{u} + \nabla\cdot w \quad &\qquad\qquad\qquad\quad = 0 \end{aligned} \tag{1}$$

These represent the momentum balance of the porous medium, the dynamic extension of Darcy's law, and conservation of fluid mass respectively. The three fields, as described above, are the skeleton displacement, u, the Darcy velocity, w and pore fluid pressure, p. The Darcy velocity, more precisely, is defined as the relative rate of volume discharge per unit area of the medium, $w = \phi(\dot{u}_{\mathrm{f}} - \dot{u})$, where $\dot{u}_{\mathrm{f}}$ refers to the absolute velocity of the fluid and ϕ is the porosity. ρ^{s} and $rhof$ are the densities of the skeleton material and the fluid, while $\rho = (1-\phi)\rho^{\mathrm{s}} + \phi\rho^{\mathrm{f}}$ is the wet density of the porous medium. K is the hydraulic conductivity of the medium and g is acceleration due to gravity. The operators ∇, $\nabla\cdot$ and $\dot{\square}$ denote gradient, divergence derivative with respect to time, and I, the 3×3 identity matrix.

In equation $(1)_1$, σ is the *effective stress* in the skeleton. The total stress in the porous medium, $\sigma^{\mathrm{t}} = \sigma - \alpha_{\mathrm{B}} pI$, where α_{B} is the Biot-Willis coefficient [23], which is commonly taken as 1 for soil material. The constitutive equation relates the effective stress to the strain, $\varepsilon = \frac{1}{2}(\nabla u + \nabla u^{\top})$. If the skeleton is modeled as isotropic and linear elastic, this constitutive equation is

$$\sigma = \frac{E}{1+\nu}(\varepsilon + \frac{\nu}{1-2\nu}\,\mathrm{trace}(\varepsilon)\,I) \tag{2}$$

where E is modulus of elasticity and ν is Poisson's ration both under the drained condition. Other constitutive equations can be used or implemented easily in MOOSE without any modifications of the poromechanics implementation itself.

Introducing, in MOOSE terms, the *auxiliary* variables,

$$v^{\mathrm{s}} = \dot{u}; \quad a^{\mathrm{s}} = \ddot{u}; \quad a^{\mathrm{f}} = \dot{w} \tag{3}$$

the set of equations (1) becomes

$$\begin{aligned} \rho a^{\mathrm{s}} \quad &+ \rho^{\mathrm{f}} a^{\mathrm{f}} \quad - \nabla\cdot\sigma + \nabla p = 0 \\ \rho^{\mathrm{f}} v^{\mathrm{s}} \quad &+ \frac{\rho^{\mathrm{f}}}{\phi}a^{\mathrm{f}} \quad + \frac{\rho^{\mathrm{f}}g}{K}w + \nabla p = 0 \\ \nabla\cdot v^{\mathrm{s}} + \nabla\cdot w \quad &\qquad\qquad\quad = 0 \end{aligned} \tag{4}$$

Equations (4) form a system of coupled partial differential equations with u, w, and p as the three unknown fields on a domain Ω. The following are appropriate boundary conditions

$$\begin{aligned} &\text{Skeleton boundary conditions} : u = u_{\mathrm{prsc}} \text{ on } \Gamma_u; \quad \sigma^{\mathrm{t}}\cdot\hat{n} = t_{\mathrm{prsc}} \text{ on } \Gamma_t \\ &\text{Fluid boundary conditions} \quad\;\; : w\cdot\hat{n} = t_{\mathrm{qrsc}} \text{ on } \Gamma_q; p = p_{\mathrm{prsc}} \text{ on } \Gamma_p \end{aligned} \tag{5}$$

where Γ_u, Γ_t, Γ_q and Γ_p are respectively the parts of boundary, Γ, of Ω, where skeleton displacement, traction, fluid flux and fluid pressure are prescribed. The corresponding prescribed values are $u_{\mathrm{prsc}}, t_{\mathrm{prsc}}, t_{\mathrm{qrsc}}$ and p_{prsc}. $\hat{n}$ is the outward unit normal to the boundary Γ.

We now proceed to develop the weak form of these equations, which is the starting point for a MOOSE implementation.

3 Weak form and mapping to kernels

To build the weak-form representation of equations (4), we multiply the three component equations by the test functions δu, dw and δp respectively. After appropriate application of integration by parts (divergence theorem), we obtain the weak form

$$\begin{aligned}
&\underbrace{\int_\Omega \rho a^{\mathrm{s}} \cdot \delta u \,\mathrm{d}\Omega}_{\substack{\texttt{InertialForce}\\ \text{with } \alpha=0}} + \boxed{\underbrace{\int_\Omega \rho^{\mathrm{f}} a^{\mathrm{f}} \cdot \delta u \,\mathrm{d}\Omega}_{\texttt{PoreFluidInertialForceCoupling}}} + \underbrace{\int_\Omega \sigma \cdot \delta\epsilon \,\mathrm{d}\Omega}_{\texttt{StressDivergenceTensors}} - \cancel{\int_{\Gamma_t} (\sigma\hat{n}) \cdot \delta u \,\mathrm{d}\Gamma} \underbrace{\left(\int_{\Gamma_t} t_{\mathrm{prsc}} \cdot \delta u \,\mathrm{d}\Gamma \right)}_{\texttt{Pressure}} \\
&- \underbrace{\int_\Omega p \nabla \cdot \delta u \,\mathrm{d}\Gamma}_{\substack{\texttt{PoroMechanicsCoupling}\\ \text{with } \alpha_{\mathrm{B}}=1}} + \cancel{\int_{\Gamma_t} p\hat{n} \cdot \delta u \,\mathrm{d}\Gamma} + \boxed{\underbrace{\int_\Omega \left(\rho^{\mathrm{f}} a^{\mathrm{s}} + \frac{\rho^{\mathrm{f}}}{\phi} a^{\mathrm{f}} + \frac{\rho^{\mathrm{f}} g}{K} w \right) \cdot \delta w \,\mathrm{d}\Omega}_{\texttt{DynamicDarcyFlow}}} \\
&- \underbrace{\int_\Omega p \nabla \cdot \delta w \,\mathrm{d}\Gamma}_{\substack{\texttt{PoroMechanicsCoupling}\\ \text{with } \alpha_{\mathrm{B}}=1}} + \boxed{\underbrace{\int_{\Gamma_p} p_{\mathrm{prsc}} \hat{n} \cdot \delta w \,\mathrm{d}\Gamma}_{\texttt{PorePressureBC}}} - \underbrace{\int_\Omega \nabla \cdot v^{\mathrm{s}} \delta p \,\mathrm{d}\Omega}_{\texttt{INSMass}} - \underbrace{\int_\Omega \nabla \cdot w \delta p \,\mathrm{d}\Omega}_{\texttt{INSMass}}
\end{aligned} \tag{6}$$

Below each term in the weak form, we show how it maps to the respective *kernel* or *boundary condition* in a MOOSE implementation. We recognize that a number of terms in the weak form map to existing MOOSE kernels and boundary conditions. The `StressDivergenceTensors`, `InertialForce` and `PoroMechanicsCoupling` kernels and the `Pressure` boundary condition belong to the `tensor_mechanics` module, while the `INSMass` kernel is from the `navier_stokes` module. We then identify two new kernels — `PoreFluidInertialForceCoupling` and `DynamicDarcyFloe`, and a new boundary condition — `PorePressureBC` (shown boxed in equation (6)) that need to be implemented for a three-field dynamic poromechanics formulation. We present their implementation in section 5. We note that the kinematic boundary conditions $u = u_{\mathrm{prsc}}$ on Γ_u and $w \cdot \hat{n} = t_{\mathrm{qrsc}}$ on Γ_q can be imposed using the `PresetBC` boundary condition in MOOSE.

4 Time discretization and auxiliary kernels

We discretize the formulation in time using Newmark's method. The strong form (4) and the (6) are expressed at time time $n+1$. In Newmark's method, the kinematics are approximated by

$$\begin{aligned}
v^{\mathrm{s}}_{n+1} &= v^{\mathrm{s}} n + (1-\gamma)\Delta t a^{\mathrm{s}}_n + \gamma \Delta t a^{\mathrm{s}}_{n+1} \\
u_{n+1} &= u_n + v^{\mathrm{s}}_n \Delta t + \left(\tfrac{1}{2} - \beta\right) \Delta t^2 a^{\mathrm{s}}_n + \beta \Delta t^2 a^{\mathrm{s}}_{n+1} \\
w_{n+1} &= wn + (1-\gamma)\Delta t a^{\mathrm{f}}_n + \gamma \Delta t a^{\mathrm{f}}_{n+1}
\end{aligned} \tag{7}$$

We follow the clever implementation of Newark's method in the `tensor_mechanics` module in MOOSE using *auxiliary kernels*. The following are defined in the existing auxiliary kernels `NewmarkAccelAux` and `NewmarkVelAux` respectively in the `tensor_mechanics` module.

$$\begin{aligned}
a^{\mathrm{s}}_{n+1} &= \frac{1}{\beta \Delta t^2} \left(u_{n+1} - u_n - v^{\mathrm{s}}_n \Delta t - \left(\tfrac{1}{2} - \beta\right) \Delta t^2 a^{\mathrm{s}}_n \right) \\
v^{\mathrm{s}}_{n+1} &= v^{\mathrm{s}} n + (1-\gamma)\Delta t a^{\mathrm{s}}_n + \gamma \Delta t a^{\mathrm{s}}_{n+1}
\end{aligned} \tag{8}$$

Following this approach, we define the following in the new auxiliary kernel `NewmarkPoreFluidAccelAux`

$$a^{\mathrm{f}}_{n+1} = \frac{1}{\gamma \Delta t} \left(w_{n+1} - w_n - (1-\gamma)\Delta t a^{\mathrm{f}}_n \right) \tag{9}$$

implemented as follows.

```
/****************************************************************/
/* MOOSE - Multiphysics Object Oriented Simulation Environment  */
/*                                                              */
/*          All contents are licensed under LGPL V2.1           */
/*             See LICENSE for full restrictions                */
/****************************************************************/


#include "NewmarkPoreFluidAccelAux.h"

template<>
InputParameters validParams<NewmarkPoreFluidAccelAux>()
{
  InputParameters params = validParams<AuxKernel>();
    params.addRequiredCoupledVar("darcyvel","Darcy Velocity");
    params.addRequiredParam<Real>("gamma","gamma parameter");
  return params;
}

NewmarkPoreFluidAccelAux::NewmarkPoreFluidAccelAux(const InputParameters &
    parameters) :
  AuxKernel(parameters),
   _w_old(coupledValueOld("darcyvel")),
   _w(coupledValue("darcyvel")),
   _gamma(getParam<Real>("gamma"))
{
}

Real
NewmarkPoreFluidAccelAux::computeValue()
{
  if (!isNodal())
    mooseError("NewmarkPoreFluidAccelAux must run on a nodal variable");

  Real af_old = _u_old[_qp];
  if (_dt == 0)
    return af_old;
  return 1.0/_gamma*((_w[_qp]-_w_old[_qp])/_dt - af_old*(1.0-_gamma));
}
```

NewmarkPoreFluidAccelAux.C

5 Kernel and boundary condition implementation

We implement the two kernels — `PoreFluidInertialForceCoupling` and `PoreFluidInertialForceCoupling`, the boundary condition — `PorePressureBC`, and the auxiliary kernel — `NewmarkPoreFluidAccelAux`, in a new module called `three_field_poromechanics`. The new kernels, boundary condition and auxiliary kernel are registered in `ThreeFieldPoromechanics.C` below.

```
#include "ThreeFieldPoromechanicsApp.h"
#include "Moose.h"
#include "AppFactory.h"

#include "NewmarkPoreFluidAccelAux.h"
#include "PoreFluidInertialForceCoupling.h"
#include "DynamicDarcyFlow.h"

template<>
InputParameters validParams<ThreeFieldPoromechanicsApp>()
{
  InputParameters params = validParams<MooseApp>();

  params.set<bool>("use_legacy_uo_initialization") = false;
  params.set<bool>("use_legacy_uo_aux_computation") = false;
  return params;
}

ThreeFieldPoromechanicsApp::ThreeFieldPoromechanicsApp(const InputParameters &
    parameters) :
    MooseApp(parameters)
{
  srand(processor_id());

  Moose::registerObjects(_factory);
  ThreeFieldPoromechanicsApp::registerObjects(_factory);

  Moose::associateSyntax(_syntax, _action_factory);
  ThreeFieldPoromechanicsApp::associateSyntax(_syntax, _action_factory);
}

ThreeFieldPoromechanicsApp::~ThreeFieldPoromechanicsApp()
{
}

// External entry point for dynamic application loading
extern "C" void ThreeFieldPoromechanicsApp__registerApps() {
   ThreeFieldPoromechanicsApp::registerApps(); }
void
ThreeFieldPoromechanicsApp::registerApps()
{
  registerApp(ThreeFieldPoromechanicsApp);
}

// External entry point for dynamic object registration
extern "C" void ThreeFieldPoromechanicsApp__registerObjects(Factory & factory)
    { ThreeFieldPoromechanicsApp::registerObjects(factory); }
void
ThreeFieldPoromechanicsApp::registerObjects(Factory & factory)
{
  registerAux(NewmarkPoreFluidAccelAux);

  registerKernel(PoreFluidInertialForceCoupling);
```

```
  registerKernel(DynamicDarcyFlow);
}

// External entry point for dynamic syntax association
extern "C" void ThreeFieldPoromechanicsApp__associateSyntax(Syntax & syntax,
    ActionFactory & action_factory) { ThreeFieldPoromechanicsApp::
    associateSyntax(syntax, action_factory); }
void
ThreeFieldPoromechanicsApp::associateSyntax(Syntax & syntax, ActionFactory &
    action_factory)
{
}
```

ThreeFieldPoromechanicsApp.C

The kernel `PoreFluidInertialForceCoupling` representing the term $\rho^f a^f \cdot \delta u$ in the weak form is implemented in `PoreFluidInertialForceCoupling.C` below.

```
/****************************************************************/
/* MOOSE - Multiphysics Object Oriented Simulation Environment  */
/*                                                              */
/*          All contents are licensed under LGPL V2.1           */
/*             See LICENSE for full restrictions                */
/****************************************************************/
#include "PoreFluidInertialForceCoupling.h"
#include "SubProblem.h"

template<>
InputParameters validParams<PoreFluidInertialForceCoupling>()
{
  InputParameters params = validParams<Kernel>();
    params.set<bool>("use_displaced_mesh") = false;
    params.addRequiredCoupledVar("fluidaccel","fluid relative acceleration
    variable");
    params.addRequiredCoupledVar("darcyvel","Darcy velocity variable");
    params.addRequiredParam<Real>("gamma","gamma parameter");
  return params;
}

PoreFluidInertialForceCoupling::PoreFluidInertialForceCoupling(const
    InputParameters & parameters)
  :Kernel(parameters),
   _rhof(getMaterialProperty<Real>("rhof")),
   _af_old(coupledValueOld("fluidaccel")),
   _w(coupledValue("darcyvel")),
   _w_old(coupledValueOld("darcyvel")),
   _w_var_num(coupled("darcyvel")),
   _gamma(getParam<Real>("gamma"))
{}

Real
PoreFluidInertialForceCoupling::computeQpResidual()
{
  if (_dt == 0)
    return 0.0;
```

```
  Real af=1/_gamma*((_w[_qp] - _w_old[_qp])/_dt - (1.0-_gamma)*_af_old[_qp]);
  return _test[_i][_qp]*_rhof[_qp]*af;
}

Real
PoreFluidInertialForceCoupling::computeQpJacobian()
{
  return 0.0;
}

Real
PoreFluidInertialForceCoupling::computeQpOffDiagJacobian(unsigned int jvar)
{
  if (_dt == 0)
    return 0.0;
  if (jvar != _w_var_num)
  return 0.0;
  return _test[_i][_qp]*_rhof[_qp]/(_gamma*_dt)*_phi[_j][_qp];
}
```

PoreFluidInertialForceCoupling.C

The kernel `DynamicDarcyFlow` representing the term $\left(\rho^{\mathrm{f}} a^{\mathrm{s}} + \frac{\rho^{\mathrm{f}}}{\phi} a^{\mathrm{f}} + \frac{\rho^{\mathrm{f}} g}{K} w\right) \cdot \delta w$ in the weak form is implemented in `DynamicDarcyFlow.C` below.

```
/****************************************************************/
/* MOOSE - Multiphysics Object Oriented Simulation Environment  */
/*                                                              */
/*          All contents are licensed under LGPL V2.1           */
/*             See LICENSE for full restrictions                */
/****************************************************************/
#include "DynamicDarcyFlow.h"
#include "SubProblem.h"

template<>
InputParameters validParams<DynamicDarcyFlow>()
{
  InputParameters params = validParams<Kernel>();
    params.set<bool>("use_displaced_mesh") = false;
  params.addRequiredCoupledVar("skeletondisp","skeleton displacement variable"
    );
    params.addRequiredCoupledVar("skeletonvel","skeleton velocity variable");
    params.addRequiredCoupledVar("skeletonaccel","skeleton acceleration
    variable");
  params.addRequiredCoupledVar("fluidaccel","fluid relative acceleration
    variable");
  params.addRequiredParam<Real>("gravity","acceleration due to gravity");
    params.addRequiredParam<Real>("beta","beta parameter");
    params.addRequiredParam<Real>("gamma","gamma parameter");
  return params;
}

DynamicDarcyFlow::DynamicDarcyFlow(const InputParameters & parameters)
  :Kernel(parameters),
   _rhof(getMaterialProperty<Real>("rhof")),
```

```
    _nf(getMaterialProperty<Real>("porosity")),
    _K(getMaterialProperty<Real>("hydconductivity")),
    _us(coupledValue("skeletondisp")),
    _us_old(coupledValueOld("skeletondisp")),
    _vs_old(coupledValueOld("skeletonvel")),
    _as_old(coupledValueOld("skeletonaccel")),
    _u_old(valueOld()),
    _af_old(coupledValueOld("fluidaccel")),
    _us_var_num(coupled("skeletondisp")),
    _gravity(getParam<Real>("gravity")),
    _beta(getParam<Real>("beta")),
    _gamma(getParam<Real>("gamma"))
{}

Real
DynamicDarcyFlow::computeQpResidual()
{
  if (_dt == 0)
    return 0.0;
  Real as=1/_beta*(((_us[_qp]-_us_old[_qp])/(_dt*_dt)) - _vs_old[_qp]/_dt -
    _as_old[_qp]*(0.5-_beta));
  Real af=1/_gamma*((_u[_qp]-_u_old[_qp])/_dt - (1.0-_gamma)*_af_old[_qp]);
  return _test[_i][_qp]*_rhof[_qp]*( as + af/_nf[_qp] + _gravity/_K[_qp]*_u[
    _qp] );
}

Real
DynamicDarcyFlow::computeQpJacobian()
{
  if (_dt == 0)
    return 0.0;
  return _test[_i][_qp]*_rhof[_qp]*(1.0/(_nf[_qp]*_gamma*_dt) + _gravity/_K[
    _qp])*_phi[_j][_qp];
}

Real
DynamicDarcyFlow::computeQpOffDiagJacobian(unsigned int jvar)
{
  if (_dt == 0)
    return 0.0;
  if (jvar != _us_var_num)
  return 0.0;
  return _test[_i][_qp]*_rhof[_qp]/(_beta*_dt*_dt)*_phi[_j][_qp];
}
```

DynamicDarcyFlow.C

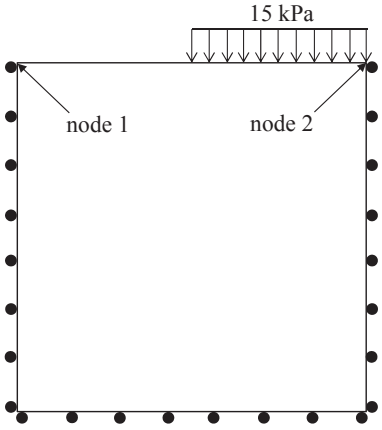

Figure 1: 2D-plane strain model for verification example

6 Verfication example

We select as verification example a 2D-plane strain model of a block of soil with a strip load on the surface. This example has been presented in [3, 24]. It is particularly interesting because we found that numerical results presented in the literature for this problem are incorrect; perhaps due to inadequate spatial discretization, they fail to even qualitatively resemble the correct solution, misestimating basic frequency and dissipation characteristics. We computed solutions for this problem using a three-field formulation and a mixed finite element approach [25], and verified them using boundary element solutions obtained using [22], which are not influenced by the resolution of domain discretization. We therefore have confidence in using these results as reference to verify our MOOSE implementation. We also computed solutions to this problem using COMSOL based on a *u-p* formulation and obtained similar results, adding further confidence; however, the COMSOL solution shows instability for low values of hydraulic conductivity.

The model is shown in Figure 1. Due to symmetry, only half of the domain is represented. Displacements perpendicular to the left, right and bottom walls are constrained. A load of 15 kPa is applied instantaneously on half of the top surface. The left, right and bottom walls are impermeable, and the fluid pressure at the top surface is zero. The properties are $E = 14.5 \times 10^3$ kPa, $\nu = 0.3$, $\rho^{\mathrm{s}} = 2700\mathrm{kg/m}^3$, $\rho^{\mathrm{f}} = 1000\mathrm{kg/m}^3$ and $\phi = 0.42$. Two values of hydraulic conductivity are used $K = 10^{-1}$ m/s and $K = 10^{-4}$ m/s. The reference solutions are shown in Figures 2 and 3.

As a first step, we consider the dynamics of the skeleton alone, without the fluid (and slightly different material properties). We model this in MOOSE using the `tensor_mechanics` module and a 20×20 grid of 4-node quadrilateral Lagrange finite elements. The input file for this model is listed in the Appendix. The MOOSE solution for the displacement of the top corner point is shown in Figure 4 together with a solution from ABAQUS using an identical finite element discretization. Since the first two frequencies of the model are close to each other, a beating phenomenon is observed. We note that there is a slight discrepancy between the MOOSE and ABAQUS solutions. This requires further exploration.

The input file for the full porous medium model using the new `three_field_poromechanics` module is also listed in the Appendix. However, the rate of convergence of the linear solver, while executing this problem is very slow, and results in instability of the solution over time. A possible reason for this is that the jacobain for the three-field formulation is a saddle point matrix, and likely requires appropriate preconditioning. This is the main issue that needs to be resolved in the remainder of this project.

7 Remaining tasks

The following tasks remain to be completed in the project.

1. Understand and resolve the numerical convergence issue in executing the dynamic poroelasticity verification example. Verify MOOSE solution using mixed finite element solution [25], boundary element solution [22] and COMSOL solution based on $u - p$ formulation.

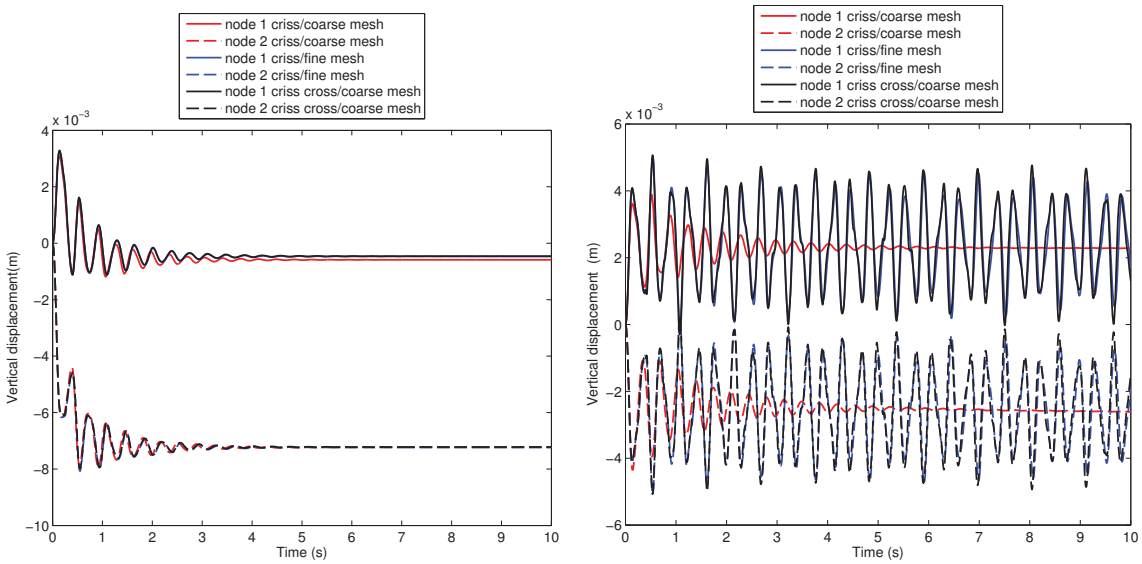

(a) $K = 10^{-1}$ (b) $K = 10^{-4}$

Figure 2: Reference solution obtained using three-field formulation and a mixed finite element approach [25]; solution for small hydraulic conductivity, K, is highly mesh-dependent; fine mesh solution agreed with boundary element solution obtained using [22]

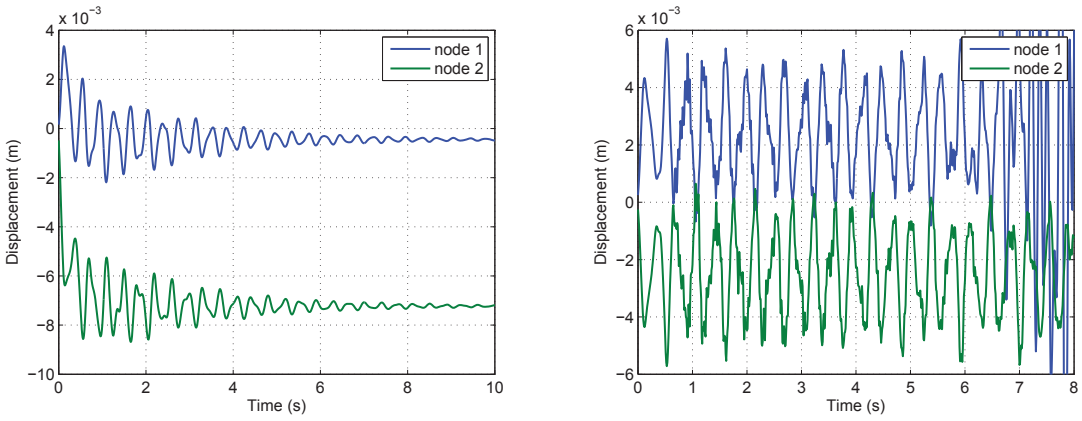

(a) $K = 10^{-1}$ (b) $K = 10^{-1}$

Figure 3: COMSOL solution using u-p formulation; solution for small hydraulic conductivity, K, shows instability

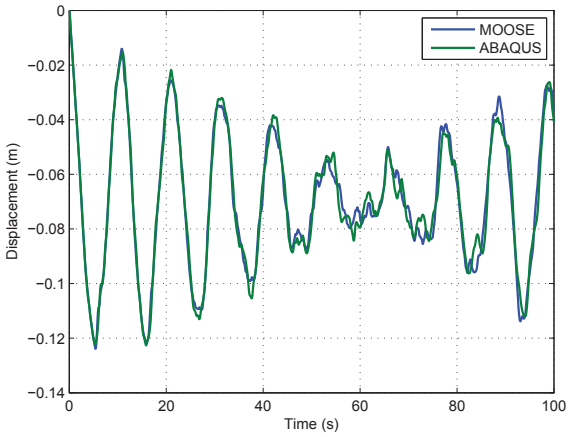

Figure 4: Displacement of top corner point in the response of the skeleton alone

2. Understand and resolve the difference between the MOOSE solution and ABAQUS solution for the solid dynamics example.

3. Implement a `ThreeFieldPoromechanicsAction` to simplify input for three-field poromechanics problems.

4. Test the implementation using additional verification examples.

5. If the use of Lagrange finite elements for u and w and lower-order monomial finite elements for p is found unsatisfactory, implement a mapping of the new kernels to vector finite elements such as Raviart-Thomas elements in libmesh for the w field.

References

[1] O. Zienkiewicz and T. Shiomi, "Dynamic behavior of saturated porous media; the generalized Biot formulation and its numerical solution," *International journal for numerical and analytical methods in geomechanics*, vol. 8, no. 1, pp. 71–96, 1984.

[2] B. Jeremić, Z. Cheng, M. Taiebat, and Y. Dafalias, "Numerical simulation of fully saturated porous materials," *International Journal for Numerical and Analytical Methods in Geomechanics*, vol. 32, no. 13, pp. 1635–1660, 2008.

[3] C. Li, R. I. Borja, and R. A. Regueiro, "Dynamics of porous media at finite strain," *Computer methods in applied mechanics and engineering*, vol. 193, no. 36, pp. 3837–3870, 2004.

[4] O. Zienkiewicz, C. Chang, and P. Bettess, "Drained, undrained, consolidating and dynamic behaviour assumptions in soils," *Geotechnique*, vol. 30, no. 4, pp. 385–395, 1980.

[5] O. Zienkiewicz, *Basic formulation of static and dynamic behavior of soil and other porous media*, pp. 39–55. Springer, 1982.

[6] O. Zienkiewicz, A. Chan, M. Pastor, D. Paul, and T. Shiomi, "Static and dynamic behaviour of soils: a rational approach to quantitative solutions. i. fully saturated problems," *Proceedings of the Royal Society of London. A. Mathematical and Physical Sciences*, vol. 429, no. 1877, pp. 285–309, 1990.

[7] M. A. Murad and A. F. Loula, "On stability and convergence of finite element approximations of Biot's consolidation problem," *International journal for Numerical Methods in Engineering*, vol. 37, no. 4, pp. 645–667, 1994.

[8] F. Oka, A. Yashima, T. Shibata, M. Kato, and R. Uzuoka, "FEM-FDM coupled liquefaction analysis of a porous soil using an elasto-plastic model," *Applied Scientific Research*, vol. 52, no. 3, pp. 209–245, 1994.

[9] Q. Zhu and J. F. Suh, "Dynamic biphasic poroviscoelastic model simulation of hydrated soft tissues and its potential applications for brain impact study," *American Society of Mechanical Engineering*, vol. 50, pp. 835–836, 2001.

[10] R. Liu, *Discontinuous Galerkin finite element solution for poromechanics*. Ph.d., 2004.

[11] J. H. Prevost, "Nonlinear transient phenomena in saturated porous media," *Computer Methods in Applied Mechanics and Engineering*, vol. 30, no. 1, pp. 3–18, 1982.

[12] M. Engelman, R. Sani, P. Gresho, and M. Bercovier, "Consistent vs. reduced integration penalty methods for incompressible media using several old and new elements," *International Journal for Numerical Methods in Fluids*, vol. 2, no. 1, pp. 25–42, 1982.

[13] J. H. Prevost, "Wave propagation in fluid-saturated porous media: an efficient finite element procedure," *International Journal of Soil Dynamics and Earthquake Engineering*, vol. 4, no. 4, pp. 183–202, 1985.

[14] R. L. Spilker and T. A. Maxian, "A mixed penalty finite element formulation of the linear biphasic theory for soft tissues," *International Journal for Numerical Methods in Engineering*, vol. 30, no. 5, pp. 1063–1082, 1990.

[15] J.-K. Suh, R. Spilker, and M. Holmes, "A penalty finite element analysis for nonlinear mechanics of biphasic hydrated soft tissue under large deformation," *International Journal for Numerical Methods in Engineering*, vol. 32, no. 7, pp. 1411–1439, 1991.

[16] P. Tasiopoulou, M. Taiebat, N. Tafazzoli, and B. Jeremić, "Solution verification procedures for modeling and simulation of fully coupled porous media: static and dynamic behavior," *Coupled Systems Mechanics*, vol. 4, pp. 67–98, 2015.

[17] P. Tasiopoulou, M. Taiebat, N. Tafazzoli, and B. Jeremić, "On validation of fully coupled behavior of porous media using centrifuge test results," *Coupled Systems Mechanics*, vol. 4, pp. 37–65, 2015.

[18] B. Simon, J.-S. Wu, and O. Zienkiewicz, "Evaluation of higher order, mixed and Hermitean finite element procedures for dynamic analysis of saturated porous media using one-dimensional models," *International Journal for Numerical and Analytical Methods in Geomechanics*, vol. 10, no. 5, pp. 483–499, 1986.

[19] A. Gajo, A. Saetta, and R. Vitaliani, "Evaluation of three and two field finite element methods for the dynamic response of saturated soil," *International Journal for Numerical Methods in Engineering*, vol. 37, no. 7, pp. 1231–1247, 1994.

[20] P. M. Gresho and R. L. Sani, "On pressure boundary conditions for the incompressible Navier-Stokes equations," *International Journal for Numerical Methods in Fluids*, vol. 7, no. 10, pp. 1111–1145, 1987.

[21] M. A. Biot, "Theory of propagation of elastic waves in a fluid saturated porous solid. I. Low frequency range," *The Journal of the Acoustical Society of America*, vol. 28, pp. 168–178, 1956.

[22] J. Chen and G. Dargush, "Boundary element method for dynamic poroelastic and thermoelastic analyses," *International Journal of Solids and Structures*, vol. 32, no. 15, pp. 2257–2278, 1995.

[23] J. R. Rice, "Elasticity of fluid-infiltrated porous solids (poroelasticity)." 2013.

[24] S. Diebels and W. Ehlers, "Dynamic analysis of a fully saturated porous medium accounting for geometrical and material non-linearities," *International Journal for Numerical Methods in Engineering*, vol. 39, no. 1, pp. 81–97, 1996.

[25] Z. Lotfian and M. V. Sivaselvan, "Cell volume control in three dimensions: Water movement without solute movement," *International Journal for Numerical Methods in Engineering*, submitted.

Appendix — input files

Input file for tensor-mechanics dynamics example

```
[Mesh]
    type = GeneratedMesh
    dim = 2
    nx = 20
    ny = 20
    xmin = 0
    xmax = 10
    ymin = 0
    ymax = 10
    elem_type = QUAD4
[]

[Variables]
    active = 'u_x u_y'

    [./u_x]
        order = FIRST
        family = LAGRANGE
    [../]
    [./u_y]
        order = FIRST
        family = LAGRANGE
    [../]
[]

[AuxVariables]
    [./v_x]
        order = FIRST
        family = LAGRANGE
    [../]

    [./v_y]
        order = FIRST
        family = LAGRANGE
    [../]

    [./a_x]
        order = FIRST
        family = LAGRANGE
    [../]

    [./a_y]
        order = FIRST
        family = LAGRANGE
    [../]
[]

[Kernels]
    active = 'stressdivx stressdivy inertia_x inertia_y'

    [./stressdivx]
```

```
        type = StressDivergenceTensors
        variable = u_x
        component = 0
        displacements = 'u_x u_y'
        use_displaced_mesh = false
    [../]

    [./stressdivy]
        type = StressDivergenceTensors
        variable = u_y
        component = 1
        displacements = 'u_x u_y'
        use_displaced_mesh = false
    [../]

    [./inertia_x]
        type = InertialForce
        variable = u_x
        velocity = v_x
        acceleration = a_x
        beta = 0.25
        gamma = 0.5
        use_displaced_mesh = false
    [../]

    [./inertia_y]
        type = InertialForce
        variable = u_y
        velocity = v_y
        acceleration = a_y
        beta = 0.25
        gamma = 0.5
        use_displaced_mesh = false
    [../]
[]

[AuxKernels]
    [./accel_x]
        type = NewmarkAccelAux
        variable = a_x
        displacement = u_x
        velocity = v_x
        beta = 0.25
        execute_on = timestep_end
    [../]

     [./accel_y]
        type = NewmarkAccelAux
        variable = a_y
        displacement = u_y
        velocity = v_y
        beta = 0.25
        execute_on = timestep_end
    [../]
```

```
     [./vel_x]
        type = NewmarkVelAux
        variable = v_x
        acceleration = a_x
        gamma = 0.5
        execute_on = timestep_end
    [../]

     [./vel_y]
        type = NewmarkVelAux
        variable = v_y
        acceleration = a_y
        gamma = 0.5
        execute_on = timestep_end
    [../]
[]

[Materials]
    [./elasticity_tensor]
        type = ComputeIsotropicElasticityTensor
        youngs_modulus = 1.0
        poissons_ratio = 0.3
        block = 0
    [../]

    [./strain]
        type = ComputeSmallStrain
        displacements = 'u_x u_y'
        block = 0
    [../]

    [./stress]
        type = ComputeLinearElasticStress
        block = 0
    [../]

    [./density]
        type = GenericConstantMaterial
        block = 0
        prop_names = 'density'
        prop_values = '0.1'
   [../]
[]

[Functions]
    active = 'bc_func'

    [./bc_func]
        type = ParsedFunction
        value = 'if(x<5.0,0.0,10.0)'
    [../]
[]
```

```
[BCs]
    [./bottom_y]
        type = PresetBC
        variable = u_y
        boundary = 'bottom'
        value = 0
    [../]

    [./top_y]
        type = Pressure
        variable = u_y
        boundary = 'top'
        component = 1 #y
        factor = 1.0
        function = bc_func
        use_displaced_mesh = false
    [../]

    [./left_x]
        type = PresetBC
        variable = u_x
        boundary = 'left'
        value = 0
    [../]

    [./right_x]
        type = PresetBC
        variable = u_x
        boundary = 'right'
        value = 0
    [../]
[]

[Executioner]
    type = Transient
    solve_type = 'PJFNK'
    l_max_its = 20
    nl_max_its = 10
    l_tol = 1.0e-7
    nl_rel_tol = 1.0e-12
    start_time = 0
    end_time = 100
    dtmax = 0.1
    dtmin = 0.1
    [./TimeStepper]
        type = ConstantDT
        dt = 0.1
    [../]
[]

[Outputs]
    exodus = true
    output_on = 'timestep_end'
    [./console]
```

```
        type = Console
        perf_log = true
        execute_on = 'initial timestep_end failed nonlinear'
    [../]
[]
```

Input file for for three-field-poromechanics example

```
[Mesh]
    type = GeneratedMesh
    dim = 2
    nx = 50
    ny = 50
    xmin = 0
    xmax = 10
    ymin = 0
    ymax = 10
    elem_type = QUAD4
[]

[Variables]
    [./u_x]
        order = FIRST
        family = LAGRANGE
    [../]

    [./u_y]
        order = FIRST
        family = LAGRANGE
    [../]

    [./w_x]
        order = FIRST
        family = LAGRANGE
    [../]

    [./w_y]
        order = FIRST
        family = LAGRANGE
    [../]

    [./p]
        order = CONSTANT
        family = MONOMIAL
    [../]
[]

[AuxVariables]
    [./v_x]
        order = FIRST
        family = LAGRANGE
    [../]

    [./v_y]
```

```
        order = FIRST
        family = LAGRANGE
    [../]

    [./a_x]
        order = FIRST
        family = LAGRANGE
    [../]

    [./a_y]
        order = FIRST
        family = LAGRANGE
    [../]

    [./af_x]
        order = FIRST
        family = LAGRANGE
    [../]

    [./af_y]
        order = FIRST
        family = LAGRANGE
    [../]
[]

[Kernels]
    [./stressdiv_x]
        type = StressDivergenceTensors
        variable = u_x
        component = 0
        displacements = 'u_x u_y'
        use_displaced_mesh = false
    [../]

    [./stressdiv_y]
        type = StressDivergenceTensors
        variable = u_y
        component = 1
        displacements = 'u_x u_x'
        use_displaced_mesh = false
    [../]

    [./skeletoninertia_x]
        type = InertialForce
        variable = u_x
        velocity = v_x
        acceleration = a_x
        beta = 0.25
        gamma = 0.5
        use_displaced_mesh = false
    [../]

    [./skeletoninertia_y]
        type = InertialForce
```

```
    variable = u_y
    velocity = v_y
    acceleration = a_y
    beta = 0.25
    gamma = 0.5
    use_displaced_mesh = false
[../]

[./porefluidIFcoupling_x]
    type = PoreFluidInertialForceCoupling
    variable = u_x
    fluidaccel = af_x
    darcyvel = w_x
    gamma = 0.5
[../]

[./porefluidIFcoupling_y]
    type = PoreFluidInertialForceCoupling
    variable = u_y
    fluidaccel = af_y
    darcyvel = w_y
    gamma = 0.5
[../]

[./darcyflow_x]
    type = DynamicDarcyFlow
    variable = w_x
    skeletondisp = u_x
    skeletonvel = v_x
    skeletonaccel = a_x
    fluidaccel = af_x
    gravity = 9.81
    beta = 0.25
    gamma = 0.5
[../]

[./darcyflow_y]
    type = DynamicDarcyFlow
    variable = w_y
    skeletondisp = u_y
    skeletonvel = v_y
    skeletonaccel = a_y
    fluidaccel = af_y
    gravity = 9.81
    beta = 0.25
    gamma = 0.5
[../]

[./poromechskeletoncoupling_x]
    type = PoroMechanicsCoupling
    variable = u_x
    porepressure = p
    component = 0
[../]
```

```
    [./poromechskeletoncoupling_y]
        type = PoroMechanicsCoupling
        variable = u_y
        porepressure = p
        component = 1
    [../]

    [./poromechfluidcoupling_x]
        type = PoroMechanicsCoupling
        variable = w_x
        porepressure = p
        component = 0
    [../]

    [./poromechfluidcoupling_y]
        type = PoroMechanicsCoupling
        variable = w_y
        porepressure = p
        component = 1
    [../]

    [./massconservationskeleton]
        type = INSMass
        variable = p
        u = v_x
        v = v_y
        p = p
    [../]

    [./massconservationfluid]
        type = INSMass
        variable = p
        u = w_x
        v = w_y
        p = p
    [../]
[]

[AuxKernels]
    [./accel_x]
        type = NewmarkAccelAux
        variable = a_x
        displacement = u_x
        velocity = v_x
        beta = 0.25
        execute_on = timestep_end
    [../]

     [./accel_y]
        type = NewmarkAccelAux
        variable = a_y
        displacement = u_y
        velocity = v_y
```

```
        beta = 0.25
        execute_on = timestep_end
    [../]

     [./vel_x]
        type = NewmarkVelAux
        variable = v_x
        acceleration = a_x
        gamma = 0.5
        execute_on = timestep_end
    [../]

     [./vel_y]
        type = NewmarkVelAux
        variable = v_y
        acceleration = a_y
        gamma = 0.5
        execute_on = timestep_end
    [../]

    [./fluidaccel_x]
        type = NewmarkPoreFluidAccelAux
        variable = af_x
        darcyvel = w_x
        gamma = 0.5
        execute_on = timestep_end
    [../]

    [./fluidaccel_y]
        type = NewmarkPoreFluidAccelAux
        variable = af_y
        darcyvel = w_y
        gamma = 0.5
        execute_on = timestep_end
    [../]
[]

[Materials]
    [./elasticity_tensor]
        type = ComputeIsotropicElasticityTensor
        youngs_modulus = 14.5e3
        poissons_ratio = 0.3
        block = 0
    [../]

    [./strain]
        type = ComputeSmallStrain
        displacements = 'u_x u_y'
        block = 0
    [../]

    [./stress]
        type = ComputeLinearElasticStress
        block = 0
```

```
    [../]

    [./density]
        type = GenericConstantMaterial
        block = 0
        prop_names = density
        prop_values = 1986
    [../]

    [./rhof]
        type = GenericConstantMaterial
        block = 0
        prop_names = rhof
        prop_values = 1000
    [../]

    [./porosity]
        type = GenericConstantMaterial
        block = 0
        prop_names = porosity
        prop_values = 0.42
    [../]

    [./hydconductivity]
        type = GenericConstantMaterial
        block = 0
        prop_names = hydconductivity
        prop_values = 0.1
    [../]

    [./biotcoeff]
        type = GenericConstantMaterial
        block = 0
        prop_names = biot_coefficient
        prop_values = 1.0
    [../]
[]

[Functions]
    active = 'bc_func'

    [./bc_func]
        type = ParsedFunction
        value = 'if(x<5.0,0.0,15.0)*if(t<0.1,10*t,1.0)'
    [../]
[]

[BCs]
    [./bottom_y]
        type = PresetBC
        variable = u_y
        boundary = 'bottom'
        value = 0
    [../]
```

```
    [./top_y]
        type = Pressure
        variable = u_y
        boundary = 'top'
        component = 1 #y
        factor = 1.0
        function = bc_func
        use_displaced_mesh = false
    [../]

    [./left_x]
        type = PresetBC
        variable = u_x
        boundary = 'left'
        value = 0
    [../]

    [./right_x]
        type = PresetBC
        variable = u_x
        boundary = 'right'
        value = 0
    [../]

    [./fluidbottom_y]
        type = PresetBC
        variable = w_y
        boundary = 'bottom'
        value = 0
    [../]

    [./fluidleft_x]
        type = PresetBC
        variable = w_x
        boundary = 'left'
        value = 0
    [../]

    [./fluidright_x]
        type = PresetBC
        variable = w_x
        boundary = 'right'
        value = 0
    [../]
[]

[Preconditioning]
  active = 'smp'

  [./smp]
    type = SMP
    full = true
    petsc_options_iname = '-ksp_type -pc_type -snes_atol -snes_rtol -snes_max_it -ksp_atol -ksp_rtol
```

```
    petsc_options_value = 'gmres bjacobi 1E-10 1E-10 10 1E-15 1E-10'
  [../]

  [./fdp]
     type = FDP
     full = true
   [../]
[]

[Postprocessors]
   [./cornerdisp]
     type = PointValue
     point = '10 10 0'
     variable = u_y
   [../]
[]


[Executioner]
    type = Transient
    solve_type = 'PJFNK'
    l_max_its = 200
    nl_max_its = 20
    l_tol = 1.0e-12
    nl_rel_tol = 1.0e-12
    start_time = 0
    end_time = 0.5
    dtmax = 0.01
    dtmin = 0.01
    [./TimeStepper]
        type = ConstantDT
        dt = 0.01
    [../]
[]

[Outputs]
    exodus = true
    output_on = 'timestep_end'
    [./console]
        type = Console
        #perf_log = true
        execute_on = 'initial timestep_end failed nonlinear' # linear
    [../]
    [./csv]
        type = CSV
        execute_on = 'initial timestep_end'
    [../]
[]
```